A dual numerical-experimental approach for modeling wear of Diamond Impregnated Tools

A. Quacquarelli, G. Mollon, T. Commeau, Nicolas Fillot

Version of Record: https://www.sciencedirect.com/science/article/pii/S0043164821001526
Manuscript_ad0a84cf0e6972269298d82b6b24e441

A dual numerical-experimental approach for modeling wear of Diamond Impregnated Tools

A. Quacquarelli[1], G. Mollon[1], T. Commeau[2], N. Fillot[1*]
[1] Univ Lyon, INSA-Lyon, CNRS UMR5259, LaMCoS, F-69621, France
[2] Umicore Specialty Powders France, 38100, Grenoble, France
*Corresponding author: nicolas.fillot@insa-lyon.fr

ABSTRACT

We propose a multiscale model able to predict the wear of the metallic surface used as the matrix in Diamond Impregnated Tools, considering the tribological interactions involved in the process. In the first stage of the contact, debris grains detach from the concrete due to the diamonds cutting ability and start to circulate in the contact zone where, in contact with water, they generate a slurry that defines the third body of the system and is able to abrade the matrix. At the scale of the interface, we treat the slurry bed as an equivalent fluid flowing with well-defined rheological properties. At the microscale, we discretize the wear as the sum of wear contributions due to each debris particle. This multiscale approach allows us to write a wear equation at the scale of the interface that considers the angularity and normal local load of debris grains and the hardness of the metallic surface. The model implements the independent experimental characterization of the rheology of the slurry and the wear properties of the metallic surface. The comparison of the numerical results with experiments at the scale of the tool in terms of wear rate is very encouraging, allowing us to use that model to predict wear not only in the context of DIT but also to adapt it to other similar tribological situations consisting of the wear of a soft surface caused by a flow of harder particles.

Keywords: Three-body abrasion, Contact mechanics, Cutting tools, Wear modelling, Finite element modelling

1. Introduction

Cobalt-based alloys are widely used as binders in Diamond Impregnated Tools (DIT) to cut brittle materials. DIT include coredrills, wire saws, circular and frame sawblades. They are all used in various applications such as extraction, sizing and processing of natural stones, drilling and sawing of concrete and reinforced concrete, and road repair. Whatever the type of tool, DIT are composed of abrasive segments fixed to steel support by brazing or welding. Segments consist of randomly oriented and randomly dispersed diamond crystals embedded in a metallic matrix by a sintering process [1].

Diamonds constitute the cutting edges: during the cutting process, they are held by the metallic matrix and can indent the material to cut it. The diamond-workpiece contact, generated during diamond indentation, is responsible for the two-body contact between diamond and stone, which can wear diamond due to high mechanical and thermal loads and the hardness of the workpiece itself [2]. This contact generates the removal of particles from the workpiece, which can flow within the contact zone. Abrasive mineral particles mix with the coolant (generally water) used to carry them out from the cutting zone and form an abrasive debris flow (i.e. the slurry) able to wear the metallic surface (three-body interaction). The wear of the matrix is necessary to activate new diamonds in the cutting process. As matrix wears faster than diamonds do, we are interested only in the wear of the former because this wear rate must be controlled: the matrix has to wear at a rate compatible with the diamond pull-out [3] to attain an optimum balance between service life and free-cutting ability. For these reasons, the wear resistance of the matrix has to be adjusted to the wear speed of the diamond: if the matrix wears too fast, then the diamond capacity is not completely used; if it wears more slowly than diamonds, then the slurry cannot be carried out properly and reduces the service life of the tool [4]. The mechanical interaction between the segments and the rock is illustrated in Fig. 1. Wear is the result of a complex tribological interaction involving diamond, matrix, workpiece, and the abrasive particles from the workpiece at different scales. In the third body theory framework, a useful tool allowing us to understand the mechanical interaction in terms of the flow of matter is the tribological circuit. This concept was developed by Berthier [5] and is applicable to a wide range of tribological situations. Based on this model, as both the metallic surface and the workpiece are degradable materials, detached particles from the two surfaces

define the internal source flow Q_s of the tribological circuit. Then, particles can be ejected from the system characterizing the ejection flow Q_e.

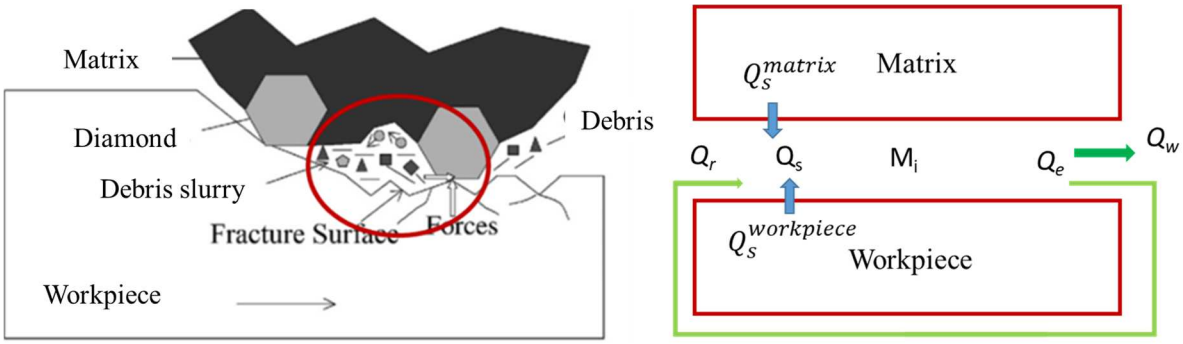

Fig. 1 Mechanical interaction at the segment-rock surface (modified from [2]);(left) and tribological circuit (right): $Q_s = Q_{s,binder} + Q_{s,workpiece}$; $Q_e = Q_r + Q_w$

Defining wear no longer as the loss of mass from one material but as the loss of mass from the whole contact [6], the wear flow Q_w is the amount of particles of Q_e that definitely leave the system, while the remaining part of Q_e defines the recirculation flow Q_r and is reintroduced in the system. Considering the mass equilibrium of the system, the amount of particles M_i of the third body per unit time is defined as:

$$\frac{dM_i}{dt} = Q_s - Q_w \tag{1}$$

As the slurry is continuously renewed and $Q_s^{workpiece} \gg Q_s^{matrix}$, steady-state is reached instantaneously and the amount of slurry that characterizes the third body is almost constant [6], [7]

$$Q_s^{workpiece} = Q_w^{workpiece} \Rightarrow M_i = const \tag{2}$$

Particles detached from the metallic surface are present in a much smaller quantity than the debris of the workpiece, such that the wear of the matrix is only due to the slurry, which characterizes the third-body of the tribosystem, and not to the metallic grains themselves.

The particular diamond-debris-matrix interaction is responsible for the complex wear mechanisms of the matrix surface. Experimental evidence shows that circular sawing and core drill behave in the same way in terms of wear patterns, even though the cutting process and the kinematics of the chip formation are different [4], [8]–[11]. In both cases, the diamond remains

in a quasi-continuous contact with the workpiece material, leading to the development of a matrix tail behind each diamond and a sort of crater in front of it (Fig. 2).

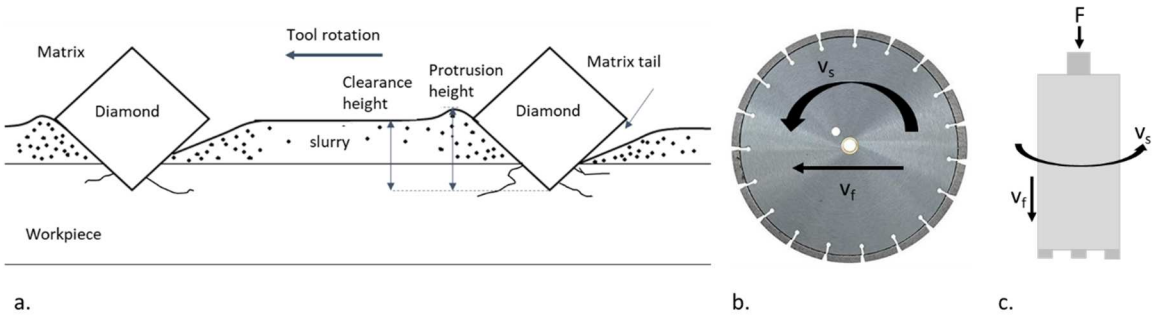

Fig. 2 a. Representation of the interactions between the tool and the workpiece during circular sawing and drilling operations (modified from [8]); b. example of circular sawing; c. example of a core drill (v_f = cutting speed; v_s = peripheral speed, F = normal load)

Such a wear process of the metallic surface depends on several aspects as:

- rock: marble, granite, concrete and reinforced concrete behave differently during processing [12] and generate a debris flow with different properties in terms of grain size (the wear rate increases with particle size until a critical value is reached, above which the wear rate seems to be independent of the grain size [13]); particle shape (freshly fractured material generates abrasives with several cutting edges able to wear faster); mineral composition and hardness (soft minerals induce slower wear mechanisms, e.g. thermal fatigue and oxidation), and cleavage properties (resistance to fragmentation) [2], [14].
- Segment specifications: the number and dimensions of the segment (at the scale of the tool), the diamond concentration (number and size of diamonds at the scale of the segment), and the matrix microstructural properties (at the scale of the matrix) [15]. In particular, at the scale of the segment, it was seen experimentally that wear around one single diamond is influenced by the presence of the other diamonds; a close diamond may offer protection and reduce the rate of the protrusion while, when the same diamond is not shielded by another one, it is fully exposed to wear [16]. Regarding the microstructure of the matrix, wear strongly depends on its material hardness.
- Operational parameters: feed rate, peripheral speed, force applied, and cooling efficiency (i.e. coolant type and flowrate) [2]. In particular, the rock processed and the coolant used exerts control on the slurry rheological properties.

Several studies have been done to analyze, at least qualitatively, the wear of the surface in terms of diamond retention after the manufacturing process [3], [17], [18], and during working conditions [19], while mechanisms involved in the matrix wear are not yet well understood. The establishment of a universal wear law remains a challenge due to the many parameters and aspects involved. The simple Archard equation [20] does not account for the changes in the wear coefficient. Siniawki et al. [21] defined a simple wear law to describe the kinetics for the abrasion for different material pairs based on the pin-on-desk. Bull and Rickerby [22] proposed a model for abrasive wear based on the multi-pass scratch test. The scratch test is nowadays widely used to determine the wear resistance of surfaces [23]–[25]. Several attempts have been made to correlate the abrasive wear to the properties of the abrasive particle (shape and size) [26]–[28], [29], [30]. Woldman et al. [25] proposed a method for predicting abrasive wear rate and understanding the wear process of machining components operating in sandy conditions. However, in all of these cases, the wear process takes place in a controlled environment and models are strictly related to the reproduced experimental test.

In the framework of cutting tools, the impossibility of considering all of the aspects involved requires a numerical study able to simplify the real phenomena. In this context, the literature is lacking in terms of numerical application. Zhou et al. [31] studied the behavior of diamond bits under drilling conditions but without considering the damage and failure; Li et al. [32] modeled the plastic deformation and residual stress close to diamond during the sintering process. More attention to the wear process is paid by Suh et al. [33], who studied the matrix wear with respect to the diamond without considering the debris flow properties on the wear process. At a smaller scale, Xu et al. [34] proposed a model to describe the failure mechanism at the diamond-matrix interface in diamond bits during failure and diamond pull out. Other models are based on mathematical and statistical multiple regressions to analyse the influence of rock properties on the matrix wear rate [9]. All of these models describe aspects of the wear process and cannot predict wear at the scale of diamond tools.

The present work is based on a new multiscale approach able to describe wear at the scale of a diamond ignoring the diamonds concentration (only one diamond is considered, which remains intact). The originality of the model proposed here consists of using an independent experimental set-up to characterize the key parameters separately. Section 2 describes the experimental-numerical approach based on the coupling between the Reynolds equation and the wear equation and implementing the aforementioned experimental tests. The results are

described in section 3. In section 4 results are discussed qualitatively and quantitatively in terms of wear rate around one diamond and the comparison between numerical and experimental results is discussed. Conclusions and new perspectives on the development of the model are given in section 5.

2. Experimental-numerical approach

The main approach is illustrated in Fig. 3. Such a method consists of three main parts and is defined by three independent experimental tests: the core drill test, the rheological test and the μ-scratch test.

The first part is based on preliminary experimental observations of the wear by performing a core-drill test. The second part deals with the numerical resolution of the Reynolds equation implementing the viscosity of the slurry obtained by a rheological test and at every location of the contact surface at the scale of the diamond. The pressure distribution controls the wear process. On the other hand, the wear equation, described in the third part of the model, will change the third body thickness profile. For a given third body thickness profile, the numerical simulation solves a strong coupling between pressure generation and surface morphology changes. This section includes a multiscale approach that starts from the experimental evidence of wear during scratching with a spherical tip indenter. It relies on the assumption that the overall wear process caused by the debris flow is the sum of wear contributions due to each debris grain that can abrade the surface as does the indenter tip during a scratch test. The coupling of the Reynolds equation and the wear equation is implemented numerically and results are compared with the experimental core-drill test to validate the model.

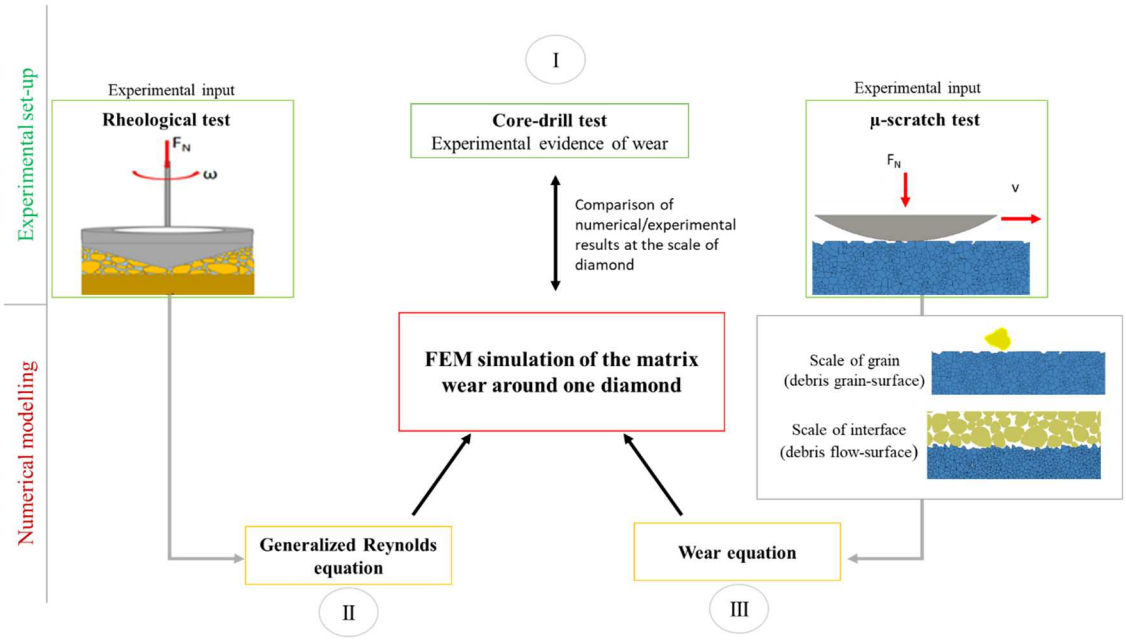

Fig. 3 The workflow of the approach

2.1 Preliminary experimental observations of wear at the diamond scale

The core-drill test is associated with non-destructive observation of diamonds on the segment in order to follow the wear of the metallic matrix during the cutting process. The tool consists of eight diamond segments brazed on a 102 mm diameter steel core barrel [35], [36], as illustrated in Fig. 2c. Diamond mesh and concentration, as well as the cutting and matrix parameters and the material to cut, are given as in Tabs. 1-2. The grain size distribution of debris grain is illustrated in Fig. 3.

Tab. 1 Main standard parameters for a drilling operation [36]

Cutting Parameters		
Tool diameter	102	mm
Metal matrix	Cobalt	
Material to be cut	Concrete	
Volume of material cut	280	cm^2
Diamond concentration*	30	
Diamond size**	40/50	mesh
Number of diamonds per segment	44	
Segment surface	91	mm^2
Number of segments	8	
Angular velocity	500	rpm
Linear (drilling) velocity	2,67	m/s
Mean cutting speed	0,4	mm/s
Applied Vertical Force	2,5	kN
Water flow	50	l/h

* 1,32 carat/cm^3 ; ** 300/375 µ

Tab. 2 Main debris and matrix parameters for a drilling operation [36]

Debris and Matrix Parameters		
Water/debris (mass ratio)	40/50	
Grain average size R_d	10	µm
Matrix grain size (before sintering)	2	µm
Matrix grain size (after sintering)	2,3	µm
Vickers Hardness	299	HV10

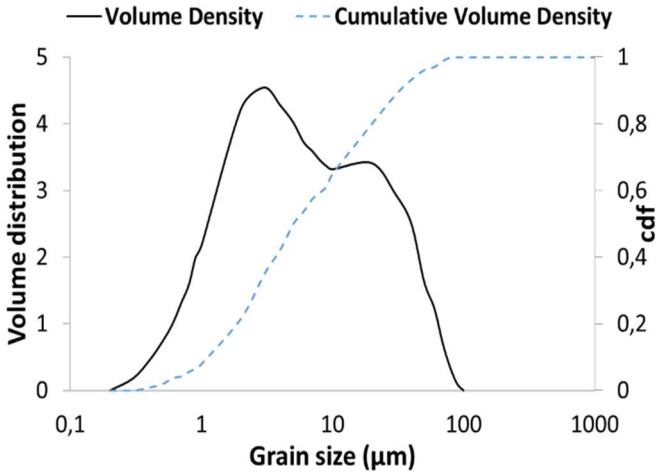

Fig. 4 Grain size distribution of debris grains diameter (The size distribution is bimodal with modes values of 20 µm and 2 µm respectively, while the main grain size is 20 µm). [36]

As introduced before, the wear of the surface around each diamond is characterized by a crater and a tail, and these results are also confirmed by the experimental test described here. In particular, the crater is characterized by two main zones: clearance and protrusion zone (C-zone and P-zone respectively in Fig. 5a). Far enough from the diamond, clearance depth h_c is defined as c_i-h_0 with h_0 the reference height on the diamond and c_i the binder level. During the cutting process, the evolution of h_c with time (Clearance Wear Rate, or CWR) represents the matrix wear rate under a linear swarf flow. The clearance allows the diamond to penetrate the material and to carry out debris. Close to the diamond in the upstream direction, protrusion depth h_p is defined as p_i-h_0 with p_i the point of the maximum depth of wear. The evolution of h_p during the cutting process (Protrusion Wear Rate, or PWR) represents the matrix wear rate under a flow disturbed by the presence of the diamond. The definition of CWR and PWR are displayed in Fig. 5b. The slurry is then able to flow around the diamond, generating a lateral zone of wear and a tail (L-zone and T-zone respectively in Fig. 4a.) before being carried out from the segment. The lateral wear rate (LWR) and the tail wear rate (TWR) are defined in the same way as the PWR and the CWR considering as reference height the diamond tip h_0.

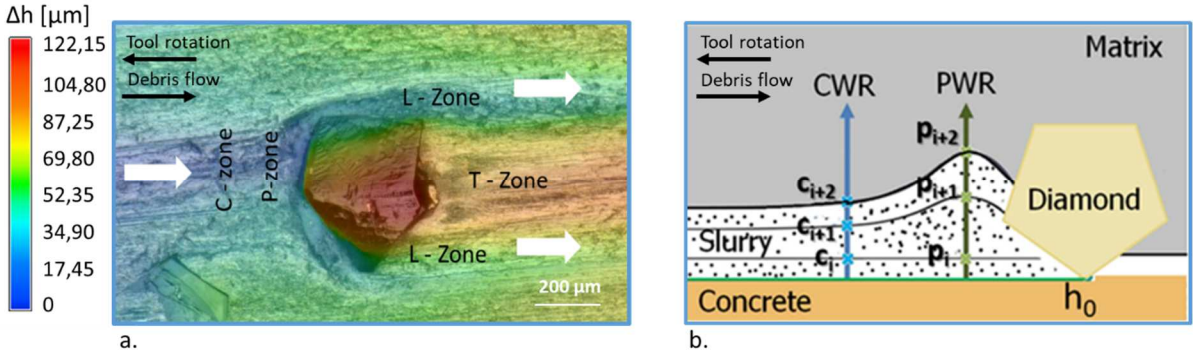

Fig. 5 Wear zones around one diamond during drilling; b. Definition of PWR and CWR [36]

Different wear mechanisms (micro-cutting, micro fatigue, micro ploughing and erosion) are involved in different proportions in the four wear zones. In the clearance zone, the main mechanisms involved are the micro-cutting (the material is removed from the surface), microcracking (the material cracks in the region surrounding the wear groove), microplouging (the material is shifted on the sides but not removed from the surface) and micro fatigue (the material is removed slowly by cyclic loading). In the protrusion zone, the predominant wear modes are micro-cutting, microcracking, and micro fatigue with some erosion processes due to the debris striking the surface. In the lateral zone, the micro fatigue mode (owing to the continuous passage of debris) and the erosion mechanism are predominant, while the tail is subjected to fatigue and blast erosion. Experimental evidence shows that erosive wear has marginal importance, secondary to the abrasion [14].

Starting from this experimental evidence, we build a numerical model able to predict the wear in the neighborhood of a diamond in terms of PWR and CWR.

2.2 Numerical modeling of the third body flow around the diamond

This section deals with the description of flow properties (i.e. pressure and velocity) at every location of the contact interface as a function of the gap thickness and the viscosity of the third body, extracted from the rheological test described in Section 3.

Experimental evidence on core-drill showed that the overall force applied to the machine is supported by diamonds to indent the workpiece [36]. Then, the debris of the cut material starts to circulate in the gap between the metallic surface and the workpiece, generating a pressure acting to the contact surface. Debris grains mixed with the coolant used to carry them out form

a slurry. This third body is treated as an equivalent fluid and studied experimentally by rheological test, discussed in the next section.

Assuming that the gap thickness of the third body (i.e. between the solid surfaces) is small enough, we solve numerically the generalized Reynolds equation [37] able to consider non-Newtonian fluid and with the idea to overcome the limitations of the classical Reynolds equation [38] dedicated to the Newtonian fluids. As detailed later, a slip velocity exists at the scale of the slurry particles with respect to the surface. However, in this continuous modeling, no-slip occurs at the interfaces between the equivalent liquid and the surfaces. In the case of thin-film without dynamic effects, we write the Navier-Stokes equations:

$$\begin{aligned} \frac{\partial p}{\partial x} &= \frac{\partial \tau_{zx}}{\partial z} \\ \frac{\partial p}{\partial y} &= \frac{\partial \tau_{zy}}{\partial z} \\ \frac{\partial p}{\partial z} &= 0 \end{aligned} \tag{3}$$

with:

$$\begin{aligned} \tau_{zx} &= \eta \cdot \dot{\gamma}_{zx} = \eta \cdot \frac{\partial u}{\partial z}; \\ \tau_{zy} &= \eta \cdot \dot{\gamma}_{zy} = \eta \cdot \frac{\partial v}{\partial z} \end{aligned} \tag{4}$$

Where η is the apparent viscosity obtained performing the rheological test. Integrating the momentum equation (3) twice and using the condition of no-slip at the wall boundary, the velocity profile along the vertical direction (z-direction) is:

$$\begin{cases} u(z) = \dfrac{\partial p}{\partial x}\left(\displaystyle\int_0^z \frac{z}{\eta} dz - \frac{\eta_e}{\eta'_e}\int_0^z \frac{dz}{\eta}\right) + \eta_e(u_2 - u_1)\displaystyle\int_0^z \frac{dz}{\eta} + u_1 \\ v(z) = \dfrac{\partial p}{\partial y}\left(\displaystyle\int_0^z \frac{z}{\eta} dz - \frac{\eta_e}{\eta'_e}\int_0^z \frac{dz}{\eta}\right) \end{cases} \tag{5}$$

Where:

$$\frac{1}{\eta_e} = \int_0^h \frac{dz}{\eta}\ ;\ \frac{1}{\eta'_e} = \int_0^h \frac{z}{\eta} dz\ ;\ \frac{1}{\eta''_e} = \int_0^h \frac{z^2}{\eta} dz \tag{6}$$

The shear rate components $\dot{\gamma}_{zx}$ and $\dot{\gamma}_{zy}$ are obtained by deriving velocity components along z, and finally, we obtain the general non –linear equation for non –Newtonian fluid:

$$\dot{\gamma}^2 = \frac{1}{\eta^2}\left\{\left[\frac{\partial p}{\partial x}\left(z - \frac{\eta_e}{\eta_e'}\right) + \eta_e(u_2 - u_1)\right]^2 + \left[\frac{\partial p}{\partial x}\left(z - \frac{\eta_e}{\eta_e'}\right)\right]^2\right\} \quad (7)$$

Where the surface velocities u_1 and u_2 define the kinematic boundary condition on the lower and upper surface.

Assuming that the slurry is an incompressible fluid, the mass-conservation equation writes:

$$\frac{\partial u}{\partial x} + \frac{\partial v}{\partial y} + \frac{\partial w}{\partial z} = 0 \quad (8)$$

Integrating Eq. (5) into Eq. (8) the generalized Reynolds equation can be written as follow:

$$\nabla \cdot (\varepsilon' \nabla p) - \frac{\partial\left[h\left(u_2 - \frac{\eta_e}{\eta_e'}\left(\frac{u_2 - u_1}{h}\right)\right)\right]}{\partial x} = 0 \quad (9)$$

Where $\varepsilon' = \left(\frac{1}{\eta_e''} - \frac{\eta_e}{\eta_e'^2}\right)$.

Eq. (9) provides the pressure distribution for a given surface topography $h(x, y)$ at a given time t. Measuring wear in terms of $h(x, y, t)$, thus leads to the variation of the pressure distribution in time, which in turn is responsible for the wear rate. Eq. (9) is written in a stationary form, as the variation of pressure is instantaneous with respect to the wear-related variation of the gap thickness $h(x, y, t)$. Therefore, the variation of the pressure with time is only due to the strong coupling between the Reynolds equation and the wear equation which is the subject of the next section.

2.3 Numerical modeling of the wear from the debris scale to the diamond scale

The model described here provides a qualitative and quantitative description of wear at the scale of diamond starting from observations at the scale of debris

The wear of the matrix surface is expressed in terms of Archard type equation [20], where the wear rate $\frac{dh}{dt}$ is related to the pressure $p(x, y)$ computed in Eq. (9) and the relative velocity u_r at the contact surface by the specific wear rate k_w :

$$\frac{dh}{dt}(x,y) = k_w \cdot p(x,y) \cdot u_r(x,y) \tag{10}$$

The strict Archard character of this equation, however, is restricted to the case where k_w is a constant. This might not always be the case, as we elaborate in the remainder of this section. It is also a straightforward notice that if the relative velocity is zero, no wear occurs at the surface. Looking at the pressure profile of the equivalent fluid $u(x,y,z)$ we identify the velocity of a single debris grain, assumed as a sphere of radius R_d, (Fig. 6) as:

$$u_d\,(x,y,R_d) = u(x,y,z) \tag{11}$$

such that the velocity of the single debris grain is computed at the center of mass of the grain itself and is equal to the velocity of the equivalent fluid at the same position. We assume here that the relative velocity u_r to consider in Eq. (10) is equal to the difference between the velocity of the surface u_{tool} and the velocity of the single grain u_d in contact with the surface (Fig. 6):

$$u_r(x,y) = u_{tool} - u_d(x,y,R_d) \tag{12}$$

This assumes that the rotation of the debris grains is negligible due to their interlocking and their angular shapes.

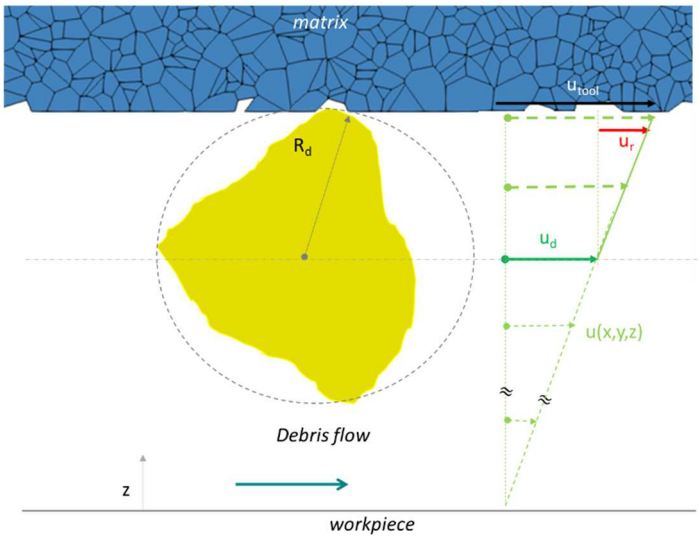

Fig. 6 Definition of the relative velocity u_r between debris and the contact surface. The surface has a sliding velocity u_{tool} and the grain of debris is moving with velocity u_d

To compute the specific wear rate k_w in Eq. (10) it is important to notice that, as illustrated in Fig. 6 and Fig. 7a., debris grains are not spherical and each of them transmits a local normal load F_d function of the contact pressure coming from Eq. (9).

The radius R_d used in Eq. (12) describes debris grains as perfectly rounded; this is a useful simplification to compute flow properties, i.e. the pressure and velocity, which involve the overall debris particle. However, generally speaking, debris grains of cut material are not spherical but show some irregularities in the shape. The angularity of abrasive particles is seldom measured quantitatively because of the difficulty of defining the main features that are responsible for the abrasiveness. However, it was seen that differences in particle shape from rounded to angular can result in differences in wear rate by a factor of 10 or more [39]. Third body particle morphologies have also been reported to control friction [40], and grain shapes exert a well-documented control on the rheology of granular plasticity and flow [41], [42]. Different methods are proposed in the literature to describe the sharpness of a particle and correlate it to the abrasive wear [43]–[45]. In this study, we use a method proposed in [46] which consists of the description of a grain contour by $n_{i,d}$ circles of different radius $r_{i,d}$ (Fig. 7b.) Then, by simple probabilistic analysis explained in Section 3, we define a characteristic radius of the asperity $r_d^* < R_d$ that controls the local features of the wear process with great influence in the macroscopic wear. The characteristic asperity behaves as an indenter tip during scratching. Assuming the perfectly plastic condition, there is no elastic recovery after the deformation. The wear volume per unit sliding distance (i.e., the cross-sectional area of the groove) is represented by the equation [30], [47], [48]:

$$V_d = \frac{r_d^{*2}}{2} \cdot (2\theta_d - \sin 2\theta_d) \tag{13}$$

This equation assumes that the shape of the scratch is conformal with the shape of the indenter, for a spherical tip, like a portion of a cylinder. In other words, the model assumes that the main abrasive wear mechanism is the cutting, i.e., all the material detached from the matrix surface is worn away and not simply displaced on the lateral edges.

The local attack angle θ_d is defined as in Fig. 7c, and writes as:

$$\theta_d = \arcsin \frac{a_d}{r_d^*} \tag{14}$$

a_d is the half contact width that can be computed considering the local characteristic asperity as an indenter able to scratch the surface under a well-defined load F_d and moving on the plane direction, such that For the aforementioned fully plastic deformation, no load-bearing supports

the rear half of the tip [49]; therefore, locally, the debris grain is in contact only over its front surface, covering a contact area equal to $\frac{\pi a_d^2}{2}$:

$$F_d = p_m \cdot \frac{\pi a_d^2}{2} \tag{15}$$

Where p_m is the mean contact pressure. It was seen experimentally [39] that, in fully plastic conditions, p_m is almost equal to the indentation hardness. During the scratch test the tip is moving in the tangential direction, this allows to consider the scratch hardness H* (assumed as representative of the hardness during multipass) equal to the mean contact pressure [30]. The way to find the scratch hardness H_s^* is discussed in the next section. For simplicity, the load F_d is assumed to be equal to the local contact pressure p(x,y) computed in Eq. (9) times the square contact surface $4R_d^2$ (Fig. 6a.):

$$F_d = p(x,y) \cdot 4R_d^2 \tag{16}$$

Obviously, this is a strong simplification of reality, allowing to shift from the local scale of debris grain contact to the global scale of interfaces contact.

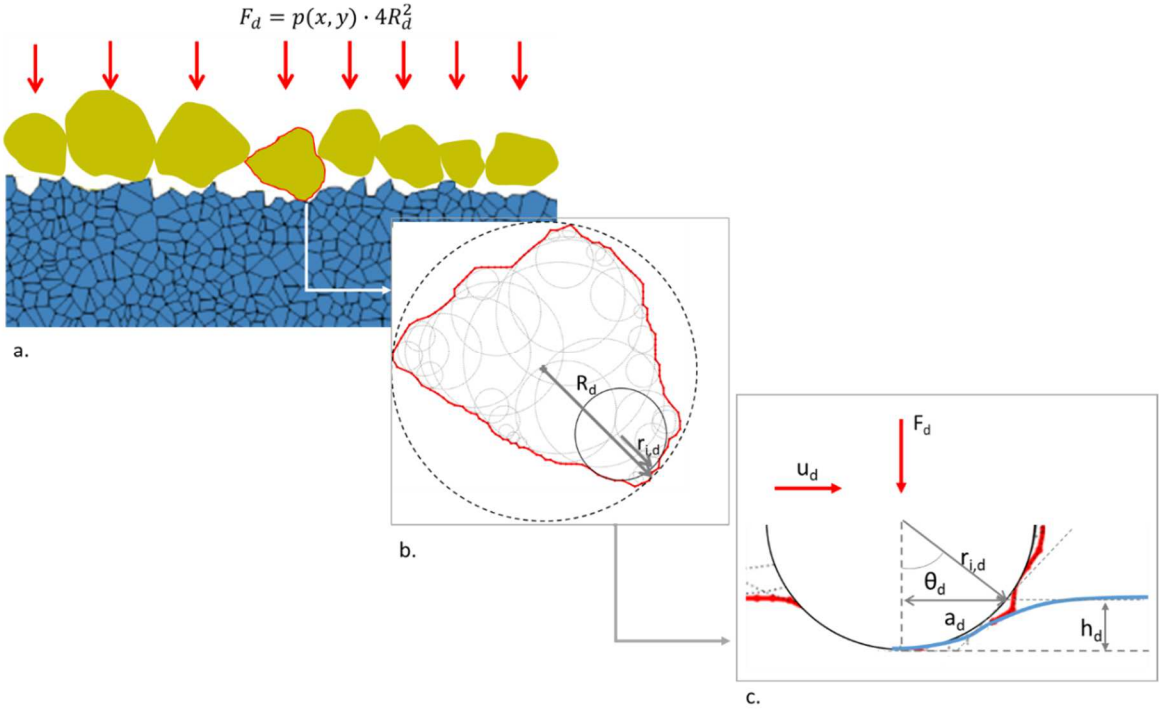

Fig. 7 a) SEM micrograph of debris particles; b) definition of roundness for a debris grain in contact with the metallic surface; c) local contact of the debris asperity and the surface

This scale jump is a key step of the model. In particular, we assume that the overall wear volume per unit sliding distance V_{slurry} related to the total amount of n individual debris grains of the

slurry passing on the surface is equal to the sum of the wear contributions V_d related to each of them, and the total normal load F_{slurry} is the sum of the normal loads F_d carried by each debris particle in contact with the matrix surface, respectively:

$$V_{slurry} = \sum_{d=1}^{n} V_d \tag{17a}$$

$$F_{slurry} = \sum_{d=1}^{n} F_d \tag{17b}$$

Then, the local wear equation at the scale of the single debris grain writes in terms of wear volume per unit sliding distance V_d and applied normal load F_d:

$$V_d = k_w \cdot F_d \tag{18}$$

Writing a_d in Eq. (15) as a function of θ_d as in Eq. (14), and then substituting Eqs. (13) and (15) in Eq. (18), the specific wear rate can be calculated as a function of the scratch hardness H_s and the attack angle θ_d:

$$k_w = \frac{(2\theta_d - \sin 2\theta_d)}{\pi \cdot \sin^2 \theta_d} \cdot \frac{1}{H_s^*} \tag{19}$$

Then, under the assumptions on Eqs. (17) the aforementioned k_w can be implemented in the wear equation Eq. (10) that is coupled with the Eq. (9) and solved numerically by FEM.

It should be noticed here that the scratch hardness is a constant for the matrix, while the angle θ_d is varying in space and time as it depends on the field of pressure that is variable along the surface and is in turn strongly coupled with the wear equation. The introduction of the pressure in the definition of specific wear rate k_w leads to an expression of the wear equation that is not a simple Archard formulation but consider also the local effect at the scale of debris grains.

2.4 Numerical procedure

Pressure and wear equations are coupled together and solved by Finite Elements in COMSOL multiphysics software. As illustrated in Fig. 8 the geometrical domain is a 3D configuration where the upper surface stands for the segment surface (matrix + diamond), the matrix is an

initially flat surface with a central diamond defined by a square-based pyramidal shape as a function of the plane coordinates (x,y). The real shape of diamond crystals ranges from the cube to the octahedron as a function of the synthesis condition [18]. For this first study, the simple octahedric shape is considered, where the part exposed to the debris flow is modeled as the square-based mentioned above. The angle $\theta_{diamond}$ in Fig. 8c can vary depending on the initial protrusion of the diamond on the surface (which also affects the ability to cut).

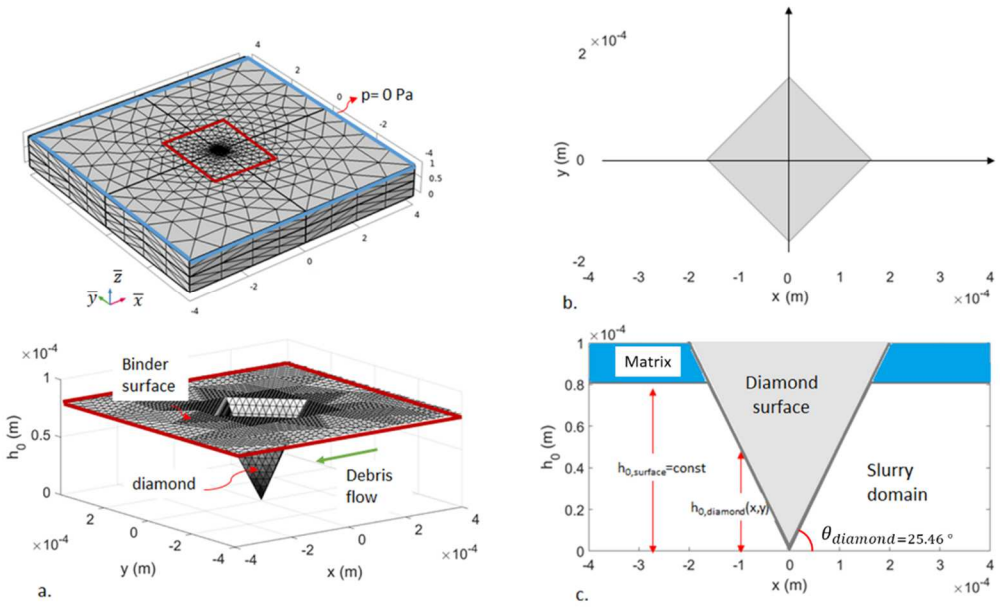

Fig. 8 a. Dimensionless domain used for the computation; b. the dimensional surface profile of the central region of interest; c. horizontal projection on the plane x-y of the surface; d. vertical projection on the plane x-z of the surface

The example shown in this case study refers to a particular diamond observed experimentally, illustrated in Fig. 9. A more detailed numerical study (including a sensitivity analysis on the shape, size, and orientation of the diamond) is an interesting perspective.

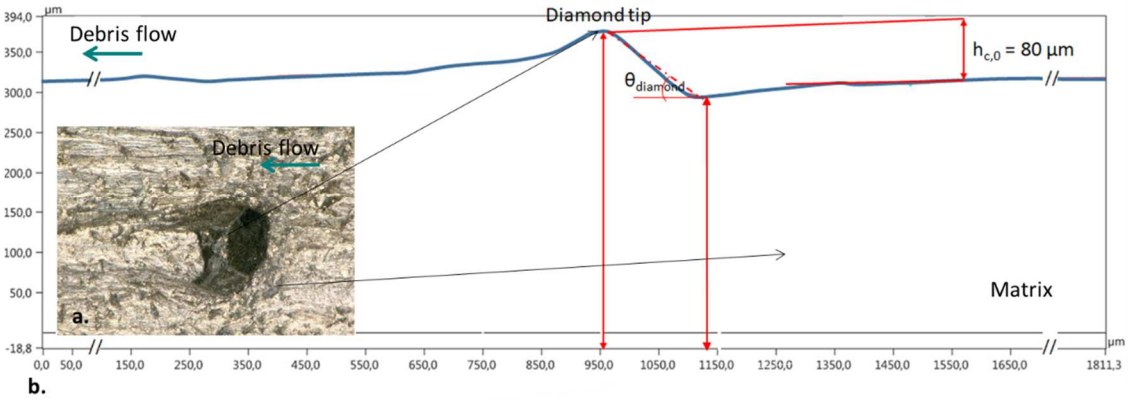

Fig. 9 Micrograpgh of a diamond embedded by the matrix. b. vertical profile of the diamond (light blue) and schematization of the geometry used in the model (red, dot line)

The 3D representation is necessary for the integration of the velocity equation and the definition of u_r in Eq. (12), while, as explained previously, the pressure profile is constant along the gap occupied by the fluid (and is thus only a 2D variable). This kind of representation allows us to define a dimensionless domain that is independent of the real size of the physical problem, as in Fig. 8a. As we are interested in the wear around the diamond and considering its particular sharpness, a finer mesh is necessary for the central part of the domain, and the smaller mesh size here is 8 µm. The domain used is much larger with respect to the surface of interest; this is a necessary choice to prevent results from being affected by the imposed boundary condition. Dirichlet boundary condition is imposed on the four lateral borders of the flat surface, as p=0 Pa.

The resolution of the wear equation in time is performed using the implicit Backward Differentiation Formula (BDF) [50], [51], which requires a convergence to attain the solution at each time step but is numerically more stable than an explicit solver. The solver uses an adaptive time step with a maximum value equal to 10 s to assure convergence. All the load applied to the machine is carried by the diamonds to cut the workpiece. The debris grains exercise pressure to the contacting surface studied numerically in terms of the Reynolds equation. The coupling between the Reynolds equation and the wear equation is explained in the flowchart in Fig. 10. The variation of pressure is instantaneous compared to the time necessary to adapt the surface at the new configuration; therefore, the variation of pressure in time is only due to the variation of the surface profile h_i. It is important to notice that, to achieve the assumption that the diamond remains intact during the process, the wear equation is applied only on the surface of the binder, therefore we have that (Fig. 7c):

$$\frac{dh}{dt} = 0 \text{ if } h(x,y,t) \geq h_{0,diamond}(x,y)$$
$$\frac{dh}{dt} = k_w(p_i) \cdot p_i \cdot u_r \text{ if } h(x,y,t) < h_{0,diamond}(x,y) \quad (20)$$

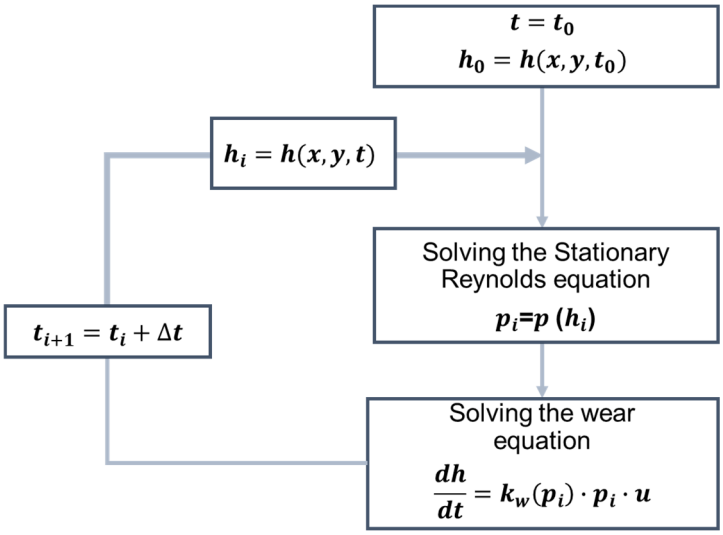

Fig. 10 Flowchart of numerical coupling between the Reynolds equation and the wear equation

3. Experimental calibration at the microscale

3.1 Rheological test

The rheological test is performed on the debris grains of concrete extracted from the drilling machine (Fig. 11) and mixed with water to reach a well-defined water/debris mass ratio (w/d = 40/50, see Tab.2).

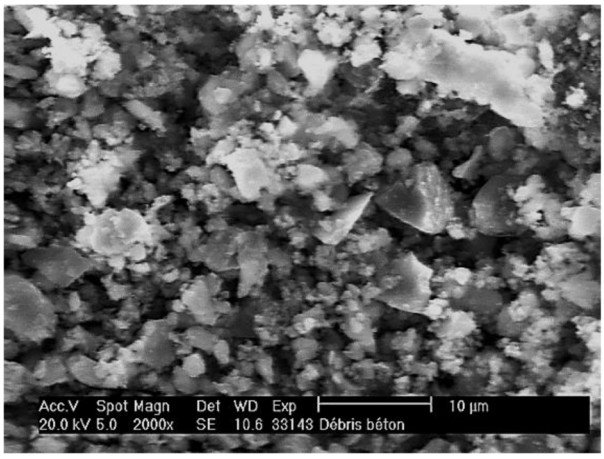

Fig. 11 SEM micrograph of debris particles [36]

Then, after shaking to re-suspend particles, the rheological test is performed using a cone and plate viscometer consisting of a flat plate and a rotating cone with a 1 mm gap thermostatically kept at 25 °C and varying the shear rate from 0.1 s^{-1} to 2000 s^{-1}. Fig. 12a plots the experimental

flow curve obtained, together with the empirical fits. The slurry shows a non-Newtonian shear thinning behavior, i.e. the apparent viscosity $\left(\eta = \frac{\tau}{\dot{\gamma}}\right)$ decreases with an increasing shear rate. This behavior, typical of pseudoplastic fluids, is also in agreement with results reported for cement slurry [52] and Coal-Water Slurry [53]. The non-Newtonian behavior may be attributed to the mechanism in which the shear stress reduces resistance to flow, orienting and distorting suspended particles in opposition to the random effect of Brownian motion.

The model that best describes the experimental dataset is the Herschel-Bulkley model:

$$\tau = \tau_0 + C|\dot{\gamma}|^n \tag{21}$$

Where τ_0 is yield stress, i.e. the stress at which the fluid starts to flow, C is the consistency index that is a simple constant of proportionality and n is the flow index, which measures the degree to which the fluid is shear thinning $(n < 1)$ or shear thickening $(n > 1)$. The Herschel-Bulkley model (HB) includes Bingham model and the Ostwald-de Wael model as particular cases considering $n = 1$ and $\tau_0 = 0$ respectively.

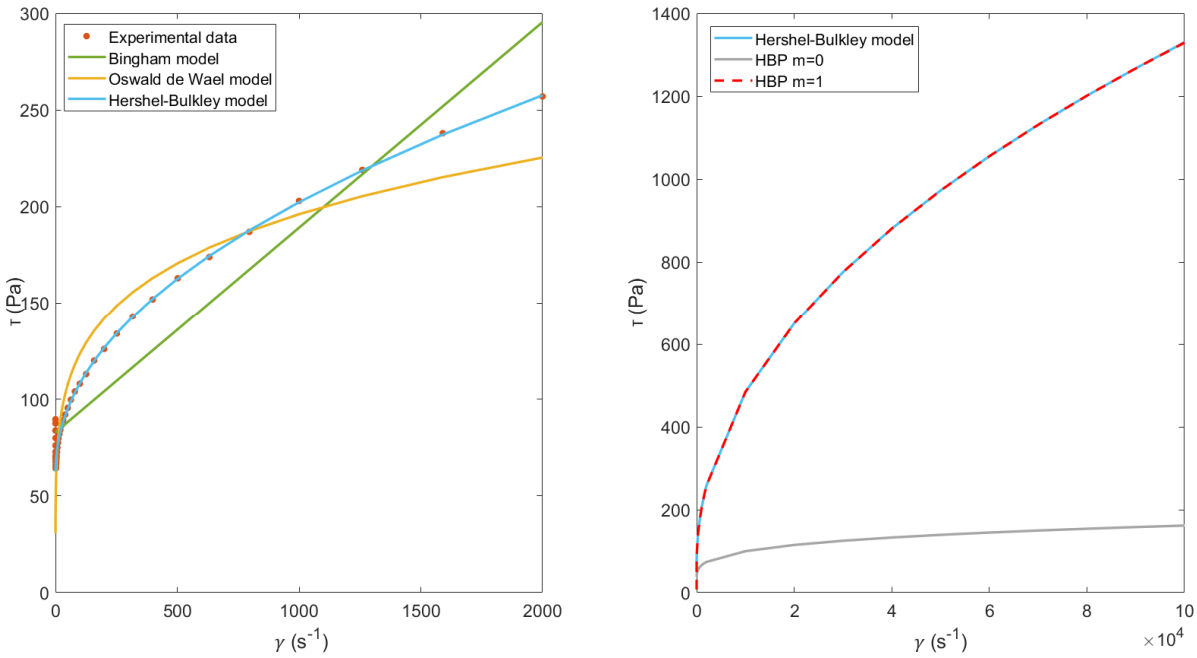

Fig. 12 a. Experimental flow curves and comparison with models fit; b. Papanastasiou regularization method applied to the Hershel Bulkley model (HBP) and comparison with the Hershel-Bulkley model

The slope change in the mathematical formulation of the law (Eq. 21) leads to some instabilities and convergence problems in the implementation of the Hershel-Bulkley model due to the change in flow regime for $\tau = \tau_0$. To solve this issue, several regularization methods are

proposed in the literature [54]–[56]. The common idea is to overcome the discontinuity due to the change in the flow regime in the yielding point using a single constitutive law holding both the yielded and the unyielded region. Using the Papanastasiou regularization [56], Eq. 21 becomes:

$$\tau = C|\dot{\gamma}|^n + \frac{\tau_0\left(1 - e^{-m|\dot{\gamma}|}\right)}{|\dot{\gamma}|} \cdot \dot{\gamma} \tag{22}$$

Where m is the regularization parameter, which reduces the singularity and makes the shear rate non-zero everywhere. If $m \to \infty$ the HBP (Hershel-Bulkley Papanastasiou) model reduces to Eq. 21, and if $m \to 0$ the model is reduced to the simple power law (Fig. 12b) The values of the shear rate observed in the application are higher than what is imposed experimentally in the rheological test ($\dot{\gamma} \geq 10^4 s^{-1}$). Assuming that the behaviour of the slurry is still described by the HB model even for a high shear rate, the regularization parameter $m = 1$ gives a good approximation of the HB model, as illustrated in Fig. 10 b.

The main parameters of the HBP model used to compute viscosity η in Eq. (9) are in Tab. 3.

Tab. 3 Parameters of the HBP model for the definition of the non-Newtonian viscosity η of the slurry

τ_0 (Pa)	C $Pa \cdot s^n$	n $(-)$	m $(-)$
61	5,26	0,48	1

3.2 Wear law: hardness characterization

Fig. 7c shows that the debris grain is able to abrade the surface under a normal load and moving in the tangential direction. This is almost the same wear process caused by an indenter during a multi-pass scratch test. Fig. 13 compares the indentation and scratch process: by definition, the scratch test can be regarded as a tangential indentation [49] where the indenter is moving and therefore in contact only over its front surface [39].

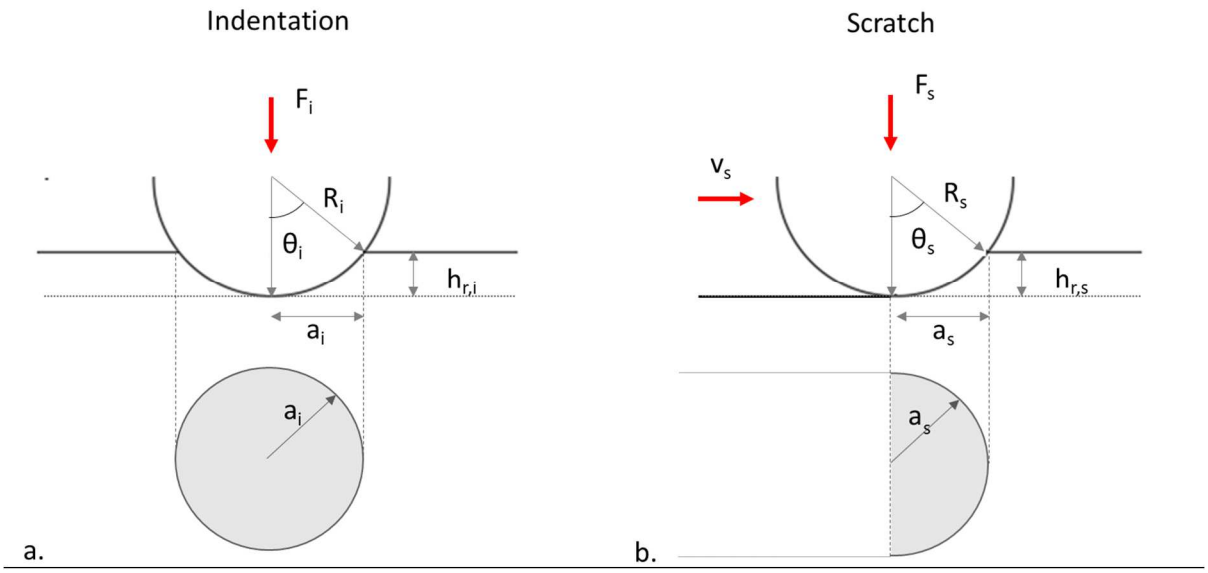

Fig. 13 Contact model between a hemispherical tip indenter and a sliding surface during a. static indentation; b. dynamic scratch. (F = normal load, v = scratch velocity; R = indenter tip radius; h_r = depth of penetration; a =half contact width; θ: attack angle).

The scratch test consists of two main steps: indentation and multi-scratch step. In the first stage of the test, a conical Rockwell diamond indenter with a spherical tip radius R_s of 100 µm penetrates in the metallic surface under a progressive load from 0.020 N to 30 N and with a scratch speed v_s of 10 mm/min for a scratch length L_s of 5 mm. The machine allows acquiring AE (acoustic emission), normal and tangential forces (and therefore the friction coefficient µ), and the depth of the scratch. During the actual indentation, the penetration depth $h_{p,s}$ is measured by depth sensors. When the load is released, post-scan observations allow defining the residual depth $h_{r,s}$: the equipment carries out a contact-sensor scan of the surface (in the same direction of the scratch) by applying a contact force as low as possible (10mN) measuring the residual depth (always less than the depth of penetration) and giving the elastic return of the material $\frac{h_{p,s}-h_{r,s}}{h_{p,s}}$. The onset load for cracking initialization and changing in wear regime is defined as critical load F_c. It is determined by optical microscopy observations and measurements of µ and AE. The modulus of critical load, as well as the wear mechanism involved, change with the mechanical properties of the material tested. In the second stage, multiple scratches are performed under constant normal load $F_s = 10\ N$ (lower than the critical load) and constant scratch velocity $v_s = 10\ mm/min$. For each scratch, we can measure the profile of $h_{p,s}$ and $h_{r,s}$, as well as µ, and we compute the mean value of indentation depth, residual depth, and coefficient of friction. From the residual depth $h_{r,s}$ we can calculate the half contact width $a_s = \sqrt{2R_s h_{r,s} - h_{r,s}^2}$ and therefore the effective attack angle θ_s and the scratch hardness defined as:

$$H_s = \frac{F_s}{\frac{\pi a_s^2}{2}} \tag{23}$$

Different abrasive wear modes can be observed during scratching, in particular, the wear mode changes from ploughing to wedge forming and then to cutting according to the increase of the attack angle, while the scratch hardness provides a good estimation of the wear resistance of the matrix under the continuous passage of debris during the cutting process.

Performing multi-scratches along the same scratch path and in the same direction provides much more information than the single scratch event in terms of damage and repeated abrasion. Also, the indentation test, as well as the single scratch test, are performed at high load leading to a high-stress abrasion process, while in the multi scratch test the load is much lower, causing less fracture damage and a low-stress abrasion process [22], [48], which is more similar to what is expected in industrial conditions. For this purpose, the scratch hardness is more representative than the Vickers's hardness in terms of wear resistance and damage. Fig. 14 plots the mean values of residual depth $h_{r,s}$, attack angle θ_s and scratch hardness H_s as a function of the number of scratches.

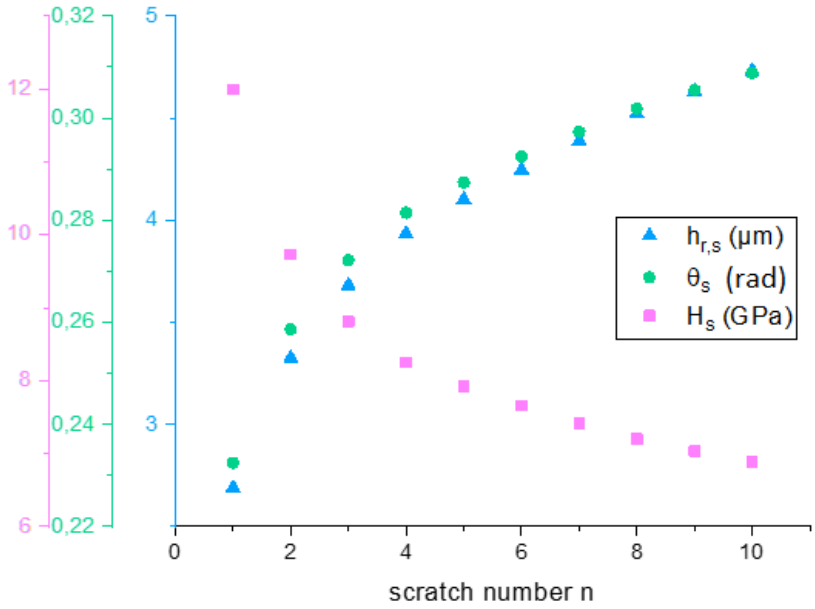

Fig. 14 Evolution of residual groove $h_{r,s}$, attack angle θ_s and scratch hardness H_s with the number of repeats scratches n

The behavior under the first scratch may be affected by initial conditions and might not be representative of the real behavior of the surface. During multi-scratches, the degree of penetration increases with the number of cycles due to the increase of the measured depth of

the groove $h_{r,s}$. For the same reason, an increase in terms of contact width is expected; as the load is constant, such behavior provides a decrease in terms of scratch hardness H_s. However, whatever is the feature, the behavior is not linear, as early scratches produce a large effect in terms of residual depth and scratch width. Then, the higher the number of pass, the smaller the effect of scratching. Hence, the cumulative effect seems to become less important when increasing the number of scratches [47]. An explanation of this trend may be the formation of an altered surface layer that characterizes the third body layer of wear particles and is able to resist further surface damage than the original material. This behavior may be also related to the plastic deformation process, such as work hardening, which is in contrast with the fatigue effect due to the multi-passing, or by the mechanical compaction of crushed material at the surface [47].

Ignoring the first pass and considering that the behavior of the metal matrix under the cutting process is more similar to what may be observed under a higher number of scratches (n>10), the characteristic scratch hardness to consider in the wear equation is calculated performing a non-linear regression of the experimental data-set. Fig. 15 shows the best fitting is the exponential function:

$$H_s = H_s^* + \Delta H_s e^{-\beta n} \tag{24}$$

Where $H_s^* = 6.39\ GPa$ is the value of scratch hardness reached after many scratch repetitions and is the characteristic value to use for the computation of k_w in the wear equation (see Eq. (15) and (19).

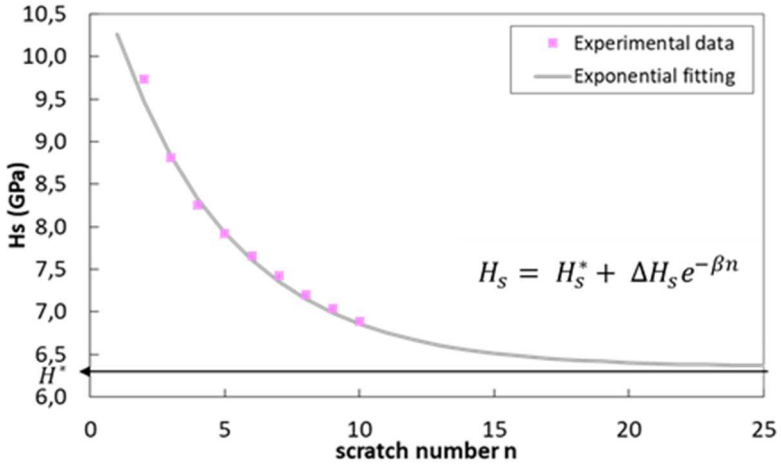

Fig. 15 Experimental scratch hardness values and exponential fitting (H_s^* = 6.39 GPa; ΔH_s = 4.906 GPa; β = 0.227)

The micro scratch test is widely used to test hard metals ([23], [47], [48], [57], [58]), and this is the reason why it is chosen to test cobalt and other alloys used as a matrix in DIT. However, the effect of the indenter tip radius on the scratch hardness is not yet well understood. Performing a single scratch pass test, different studies [59]–[61] observed that the scratch hardness increases with the reduction of the tip size, keeping the load constant. However, the scratch hardness H changes if a multipass test is performed. In this case of study, the scratch hardness is defined as the constant value reached after several passes of the indenter and the value obtained is smaller than the one after the first scratch. This procedure allows us to consider H* as an intrinsic property of the material, assuming that the metallic surface reaches a constant hardness independent of the side effect after a certain number of passes. In other words, we assume that an indenter with a tip radius equal to the characteristic asperity and under different operating conditions will reach the same value H* after a certain number of passages. This assumption allows for shifting from the scale of the experimental test to the industrial application scale.

3.3 Wear law: effect of the angularity of debris grains

A critical aspect affecting wear is the shape of abrasive particles. As explained previously, abrasive wear is strongly related to the angularity of debris grains. In order to quantify the effect of the shape of debris on the wear rate, 34 grains are extracted from Fig. 11 and analyzed considering their 2D projection (Fig. 16). After binarization and the application of a median filter to reduce the influence of noise on the contour, the shape of the real debris particle is filled with circles of radius $r_{i,d}$ applying the method originally proposed in [62] and then in [46].

Defining sharpness as a measure of the capacity of a body to cause material removal in another body by its shape alone [63], the greater abrasive power of a single grain is carried by the asperities of the contours, therefore, not all the circles that fill the grain are representative of the abrasiveness, but only those describing the local asperities. For this reason and observing that the whole radii data-set is well fitted by a lognormal distribution (Fig. 17), the characteristic value of the radius r_d^* to consider in Eqs. (13) and (14) is taken as the peak of that distribution, i.e. $r_d^* = 0.073\ \mu m$.

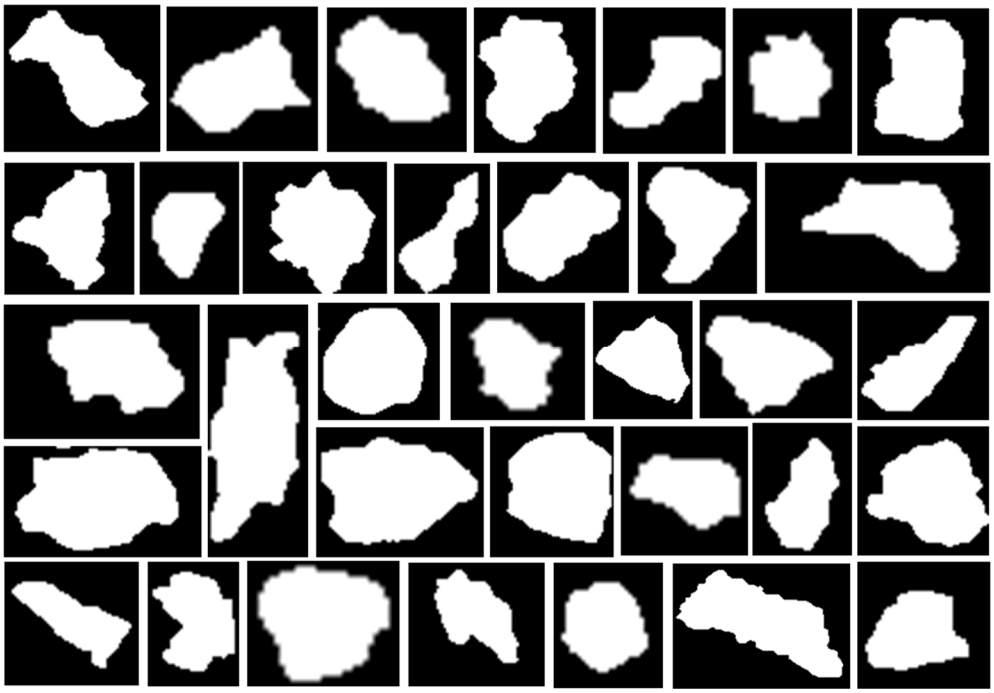

Fig. 16 Binarized debris grains extracted from the SEM scan of Fig. 11

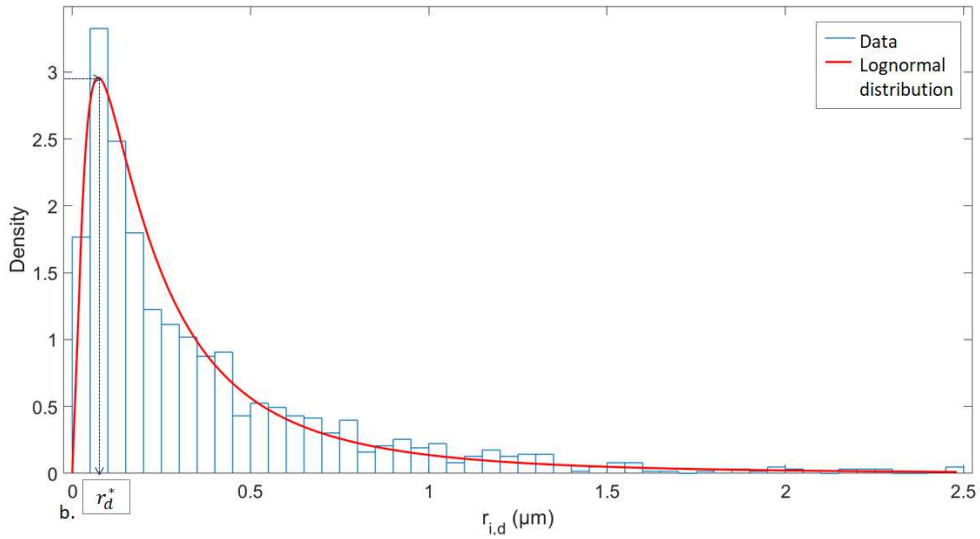

Fig. 17 Statistical analysis of circles radii $r_{i,d}$ fitted by the log-normal distribution

4. Discussion

4.1 Experimental evidence of wear

The first experimental evidence of wear using the core drill machine has been explained in Section 2 and is at the base of the model built. Analyzing in more detail the wear of the binder surface, results are in good agreement with what is observed in literature in terms of diamond retention during sawing ([9], [15], [16], [19]) and drilling [10]: starting from the emergence of

a new diamond on the bond surface, the main wear phases are the polishing, fracturing, cracking and pull out. They are well defined qualitatively and quantitatively in Fig. 18.

Emerging + Polishing phase (from t =0 s to t = 370 s in Fig. 15):

In the emerging stage, the diamond starts to emerge above the surface of the matrix, which exerts the best retention. At t = 0 s, protrusion, clearance and lateral groove are almost the same. Then, as the height of protrusion is small, the diamond cutting ability is not yet well developed. At this stage, the matrix is worn away by three-body abrasion contact allowing the whole diamond to appear with minimum surface damage and best cutting performance. Matrix wear rate is mostly linear both in terms of clearance, protrusion and lateral wear.

Micro and Macro-Fracturing phase (from t ~ 370 s to t ~ 1139 s):

During processing, the matrix is continuously subjected to abrasion and erosion in the debris removing direction until it can no longer support the diamond, which in turn starts to damage in terms of micro-cracks and micro-fractures. Wear progression leads to a completely damaged diamond. The cutting ability is reduced together with clearance and protrusion. If the diamond starts to fracture, the height of the diamond decreases with a reduction of the height of wear as it is measured in terms of the difference between the height of the matrix and the height of the diamond (Fig. 5b). For this reason, we observe the reduction of the wear rate in Fig. 18.

Pull-put phase (t > 1139 s):

The progressive reduction of the diamond retention leads to the diamond pull out, followed by the two-body abrasion between matrix and rock until new diamonds are exposed to the cutting face.

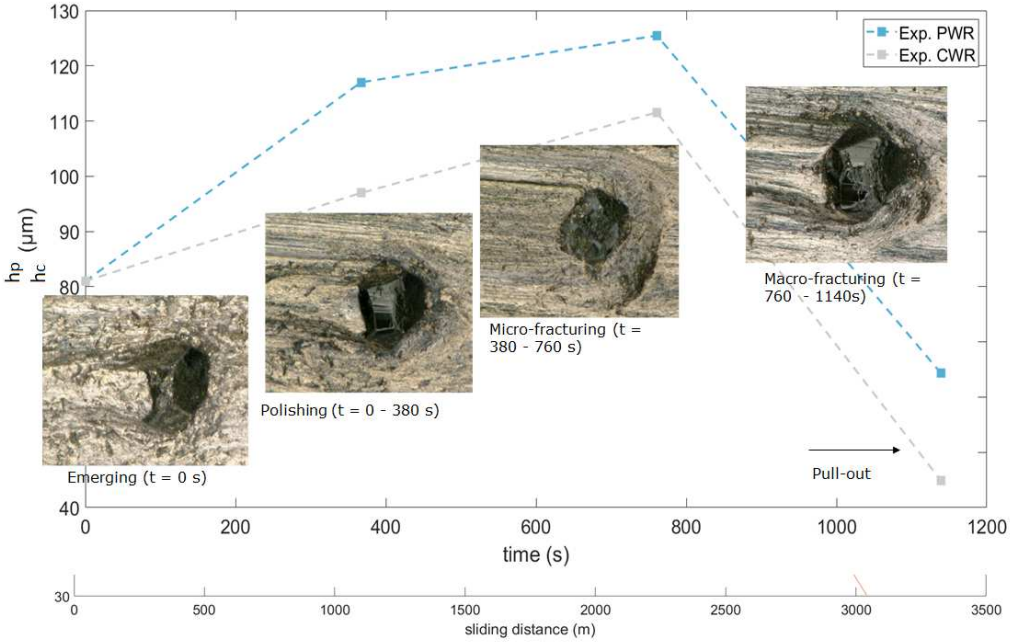

Fig. 18 Micrographs of an active diamond in a drilling process from its emerging to the pull-out (top); the evolution of its PWR, CWR, and LWR as a function of the sliding distance (sliding velocity = 2.67 m/s, see Tab. 1)

The fracturing of diamond makes difficult the measure of the relative wear depth defined in section C.1 in terms of protrusion and clearance depth (h_p and h_c respectively). For this reason, experimental measures prove a reduction in terms of wear rate in time.

As this work is focused only on the wear of the matrix, only the first polishing phase is considered as representative.

4.2 Numerical wear prediction of wear at the diamond scale

For the numerical resolution of the model, we consider the initial thickness of the slurry $h_0 = h(x, y, t_0)$ equal to the initial protrusion groove (equal to the clearance and lateral wear height) found in the experimental observation ($h_0 = 81\ \mu m$ at $t_0 = 0\ s$, see Fig. 15). Fig. 19 shows the initial 3D pressure profile on the upper surface defined as in Fig. 8. Because of the sharpness of the central diamond and the zero-pressure imposed on the boundary, the pressure has a peak close to the diamond tip and then decreases rapidly to zero to the lateral borders. It should be noticed that we consider only the part of the domain where $p > 0\ Pa$. The case $p < 0\ Pa$ is ignored, since it would induce cavitations effect, which are out of the scope of the present study [38].

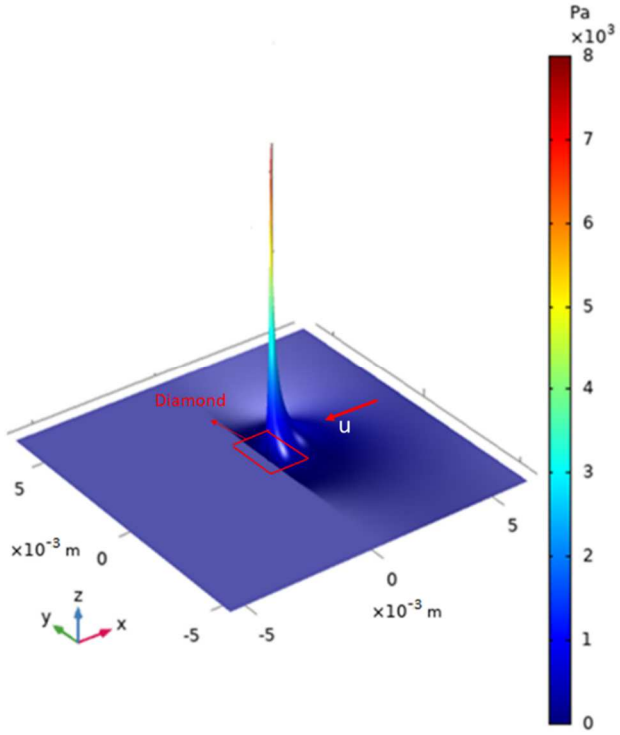

Fig. 19 Initial pressure profile at (t_0 = 0 s)

To better understand the non –linear character of the proposed wear equation, Fig. 20 plots the attack angle θ_d and the specific wear rate k_w computed as in Section 3, as a function of the pressure at the time $t_0 = 0$ s where the condition in Eq. (20) is fulfilled. As expected, k_w is not a constant in this range of pressures, indicating that the derived wear law is not strictly-speaking an Archard law.

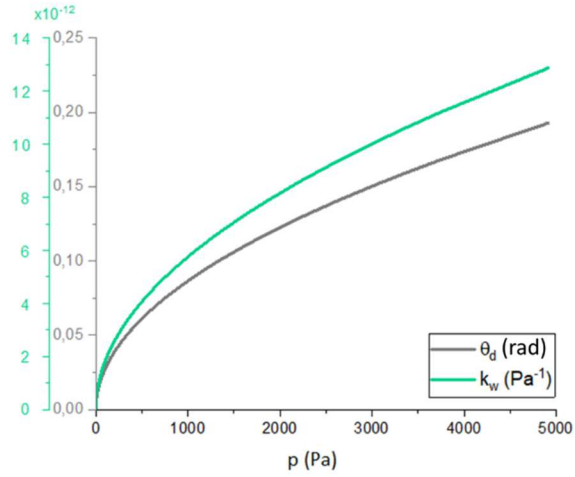

Fig. 20 Evolution on attack angle θ_d and specific wear rate k_w with pressure

The variations of k_w and θ_d are caused by the variation of the pressure along the contact surface, which in turn is strongly dependent on the geometry, as explained in the flowchart of Fig. 10:

the increase of pressure close to the diamond leads to the increase of the attack angle for the Eqs. (14-16) and therefore, for Eq. (19), an increase in terms of specific wear rate.

As introduced in Section 3.2, the attack angle controls the abrasive wear mechanisms involved in the wear process: the increase of the attack angle changes the main wear mechanism from ploughing to cutting, defining the wear zones observed in Fig. 5a and analyzed experimentally in Section 4.1. Therefore, the numerical correlation between the attack angle and the specific wear rate is justified by the experimental evidence. High values of attack angle θ_d are expected close to the diamond, in the protrusion zone, inducing a large value of specific wear rate k_w. Both the k_w and the velocity profile u_r depend on the pressure field (Eq. 19 and Eqs. 5 and 12 respectively). Fig. 21 plots the maps of k_w, p and u_r relative to the matrix surface, for $p \geq 0\ Pa$ and at same t instants of the experimental measures in Fig. 18 (for t =0 s, t = 380 and t =760 s).

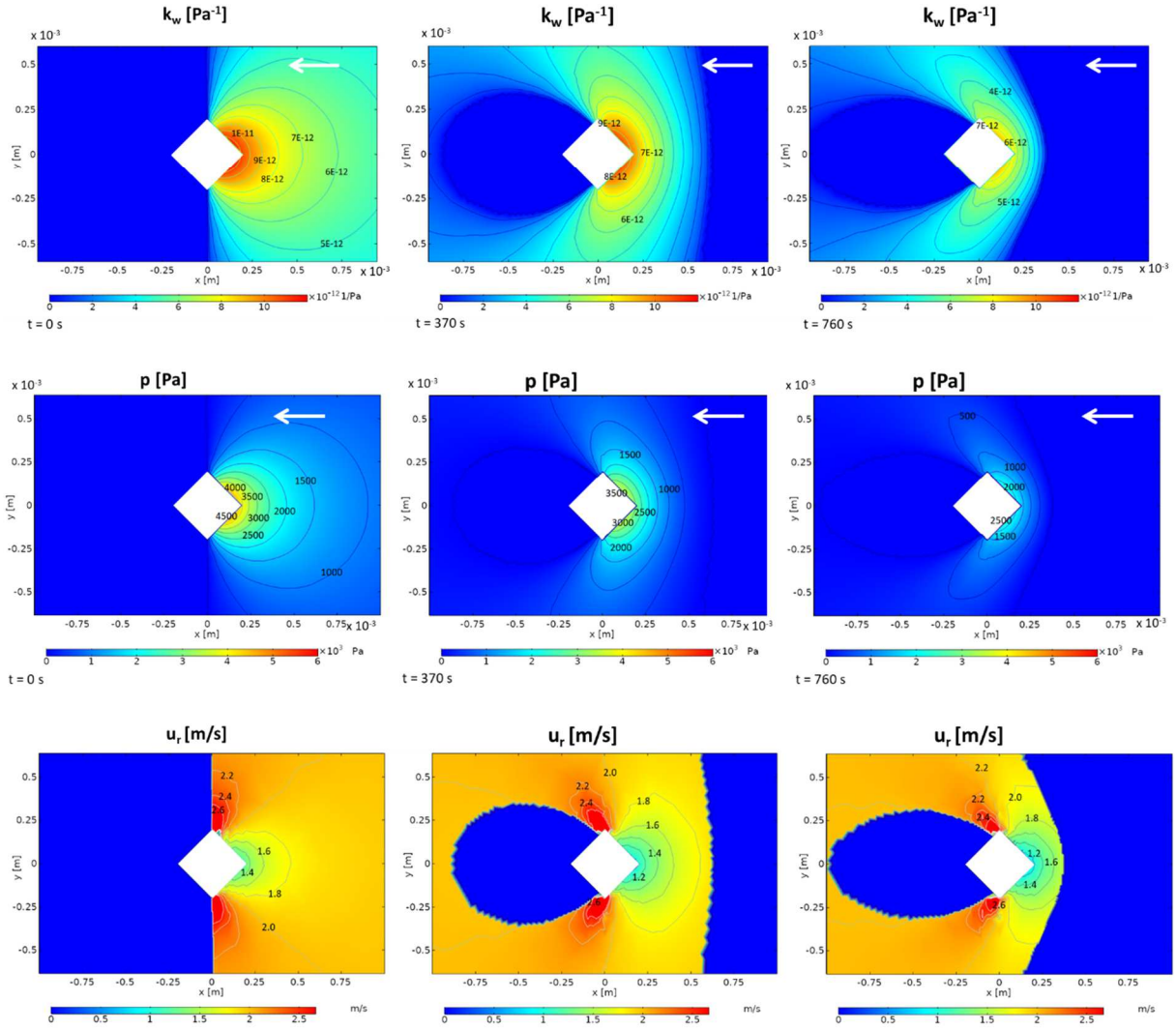

Fig. 21 Map of specific wear rate k_w (top), pressure p (centre) and relative velocity u_r (bottom) for three different times t of the simulations

At t = 0 s, the pressure field is generated instantaneously (Eq. 9), allowing calculating the u_r and k_w. The software then updates the value of Δh, which is implemented in the Reynolds equation, giving a new field of pressure and the updated k_w and u_r. During the wear process, the gap occupied by debris grains increases leading to the reduction of pressure, as observed in Fig. 21.

Fig. 22 illustrates the wear of the matrix surface for the same instants in time as the experimental measures discussed in Fig. 18. A first qualitative comparison shows that there is a good agreement in terms of PWR and CWR while the lateral flow is not well developed numerically. A possible explanation may be related to the drop of pressure on the side of the diamonds (Fig. 19 and Fig. 21) that may lead to the underestimation of k_w (Fig. 20 and Fig. 21). Fig. 21 also explains the protrusion zone close to the diamond as a function of the product between the pressure and the velocity field.

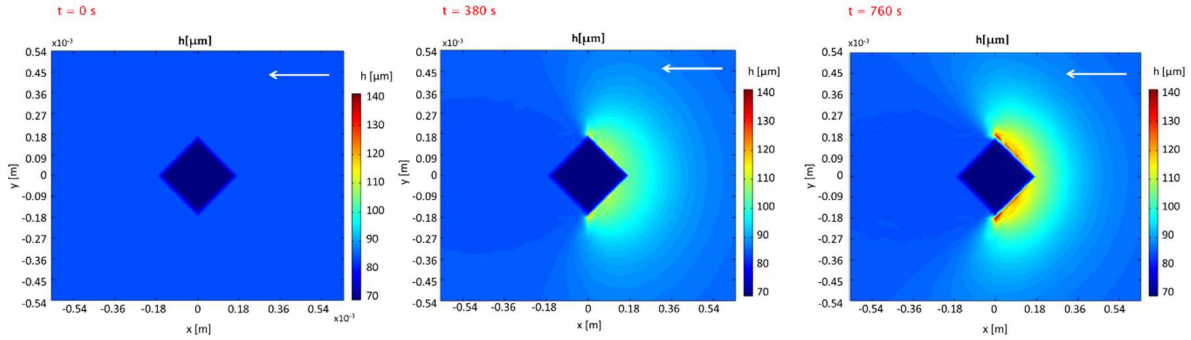

Fig. 22 Wear of the surface of the matrix computed numerically

It should be noted that one of the main assumptions of the model is that only one single diamond is considered as active in the process and the overall surface is still intact in the early stage of indentation. It means that the model ignores the previous history of wear as well as the diamond concentration and distribution. The surface of the segment is more complex than what is modeled numerically. Also, the fatigue effect due to the continuous passage of debris grains may be not completely well defined numerically.

4.3 Comparison of experimental and numerical results

The qualitative matching in terms of PWR and CWR is nevertheless confirmed quantitatively before diamonds start to fracture, as plotted in Fig. 23. This good agreement is quite remarkable, given that all the physical parameters of the model were calibrated by independent experimental tests (i.e. scratch test, rheological test, and angularity characterization).

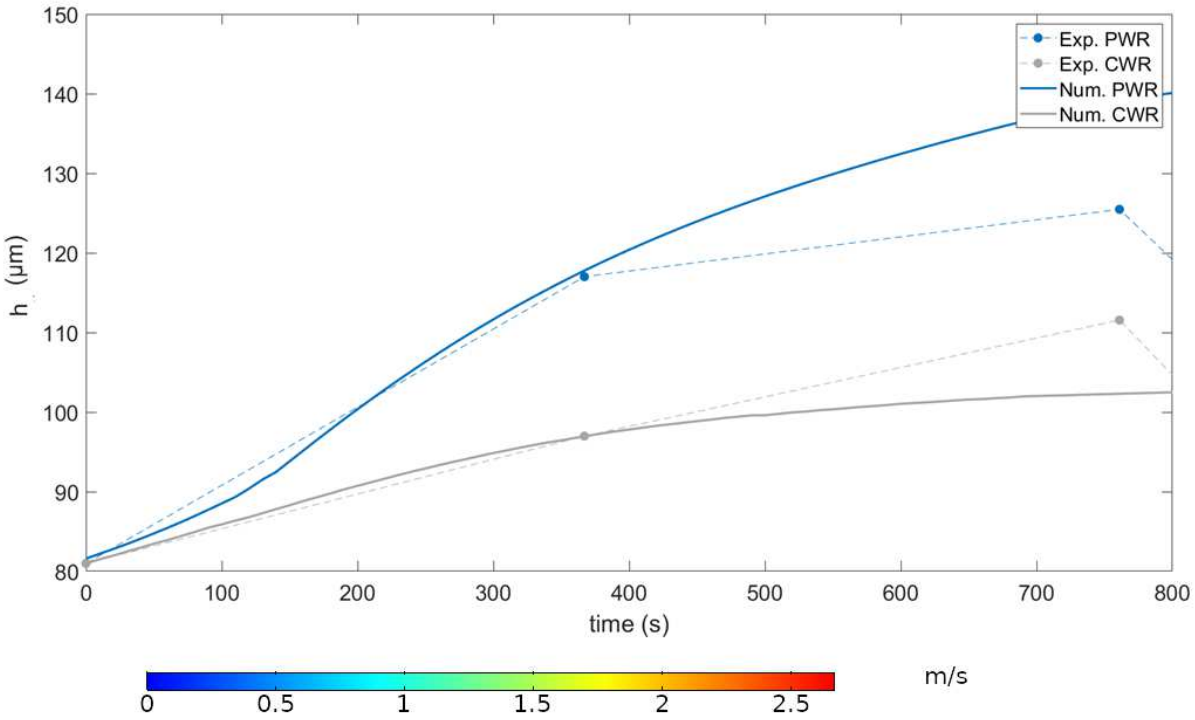

Fig. 23 Comparison between numerical and experimental PWR and CWR

As discussed previously, the diamond is considered intact during the whole cutting process, therefore we do not observe the reduction of the numerical wear rate beyond 1000-1500 m of sliding and the dramatic drop beyond 2000m. Also, after reaching a peak, the pressure slightly decreases with time because of the development of the groove on the surface. This leads to a slight reduction of the numerical wear rate that may reach a plateau as $\frac{dh}{dt} \to 0$ if $p \to 0$ for Eq. (10). As the aim of this study is the wear analysis and prediction of the binder, we restrict our focus on the first stage of diamond retention where a quasi-constant wear rate is experimentally expected and numerically confirmed.

Three different diamonds extracted from the same segment are analyzed experimentally in terms of wear rate. The average PWR and CWR are plotted in Fig. 24 for the first polishing stage together with numerical results discussed in the previous section.

The model slightly underestimates the CWR. Therefore, keeping in mind that the optimum balance between free-cutting ability and wear of the surface can be reached by looking at the ratio between the PWR and the CWR [35], the model slightly overestimates that ratio.

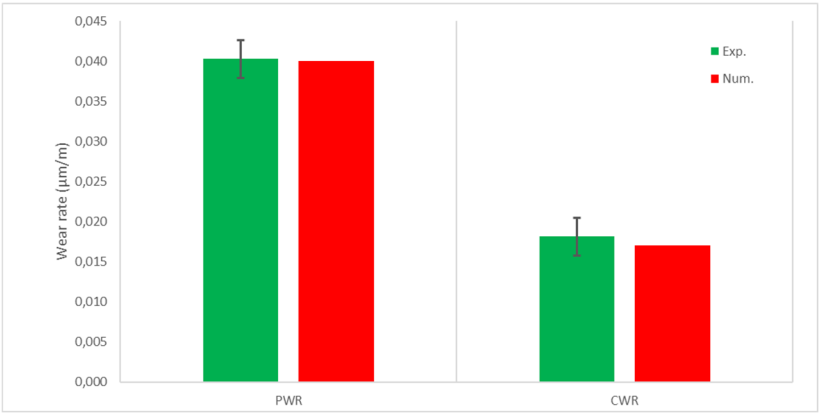

Fig. 24 Comparison between experimental and numerical wear rate in the early stage of cutting

As shown in Tab. 4, that ratio is about 1.87 and 2.35 for the experimental and numerical parts respectively.

Despite the simplifying assumptions on which the model is based, the wear in front of the diamond is well-defined both qualitatively and quantitatively as the ratio PWR/CWR is not very far from that observed experimentally. It proves that the model can provide a satisfactory prediction of the wear of the binder considering only the flow properties of the slurry, the mechanical properties of the metallic surface and the typical morphology of the debris grains. This approach is performed without any a posteriori back-calibration on drilling tests, and can thus be used with a certain level of confidence for DIC tools design.

Tab. 4 Numerical and experimental wear rate in terms of PWR and CWR

	PWR (µm/m)	CWR (µm/m)	PWR/CWR
Experimental	0,040 (+/-0,003)	0,018 (+/-0,002)	1,87 (+/-0,10)
Numerical	0,040	0,017	2,35

5. Conclusions

A new numerical model able to study the wear rate of DIT is presented here. The results obtained on a cobalt-based alloy with a well-defined slurry are in good agreement with the experimental observation of the material surface after the drilling process. The agreement is both qualitative in terms of the wear patterns on the surface and quantitative in terms of PWR and CWR. It proves that starting from an independent experimental setup consisting of a scratch test, a rheological test, and morphological characterization, and making some physically sound scale changes, it is possible to describe and predict wear at the scale of the industrial application.

The first scale jump from scratch test to grain contact is assumed at equivalent mean pressure considering the scratch hardness as a property of the metallic surface. The second jump from the local to global contact allows us to compute the specific wear rate considering that the wear of the surface is due to the contribution of each debris grain and treating the slurry as equivalent fluid flow. The specific wear rate is a function of the local pressure exerted by debris grains, it increases with the abrasiveness of debris and decreases with the increase of the hardness of the surface. The sharpness of debris grain has a strong influence on the wear of the matrix. It should be noted that the indenter used in the scratch test is a Rockwell with a perfectly spherical tip of radius 100 µm. It is therefore one order of magnitude larger than the radius of the abrasives and at least two orders of magnitude larger than their typical asperities. Another important aspect is that, at the scale of the diamond, no relative velocity is considered between the slurry (treated here as an equivalent fluid) and the matrix surface. The slip effect is considered looking at the scale of the debris grain in contact with the surface.

The geometrical model consisting of a single square-based central diamond is a strong simplification of the reality. However, experimental evidence shows that the wear is much more affected by the mechanical properties of the surface than by the geometry of the diamonds. Diamonds retained by the same metallic binder but with differences in terms of orientation, size and early height of indentation appear to have comparable wear rate.

The numerical study presents some limitations in the prediction of the lateral wear, which can be overcome considering the presence of other diamonds and a realistic topography of the segment surface, or by improving some of the basics assumptions. However, results are quite satisfactory in terms PWR and CWR, meaning that the complex phenomena can be well described numerically by this multiscale approach. Also, the correlation between pressure, attack angle and wear rate is not only consistent with the physics of the cutting process of DIT, but may also be generalized to other situations where abrasive particles have different normal loads. A great challenge is also to adapt the model to other tribological situations consisting of the wear of a soft surface caused by a flow of harder particles.

Acknowledgment

This work is supported by Umicore Specialty Powders France, for which the authors are grateful.

References

[1] J. D. Dwan, “Production of Diamond Impregnated Cutting Tools,” *Powder Metall.*, vol. 41, no. 2, pp. 84–86, Jan. 1998, doi: 10.1179/pom.1998.41.2.84.

[2] R. M. Goktan and N. Yılmaz, “Diamond Tool Specific Wear Rate Assessment in Granite Machining by Means of Knoop Micro-Hardness Process Parameters,” *Rock Mech. Rock Eng.*, vol. 50, pp. 1–17, May 2017, doi: 10.1007/s00603-017-1240-0.

[3] J. Konstanty, “Factors Affecting Diamond Retention in Stone Sawblade Segments,” *Key Eng. Mater. - KEY ENG MAT*, vol. 250, pp. 13–20, Sep. 2003, doi: 10.4028/www.scientific.net/KEM.250.13.

[4] H. K. Tönshoff, H. Hillmann-Apmann, and J. Asche, “Diamond tools in stone and civil engineering industry: cutting principles, wear and applications,” *Diam. Relat. Mater.*, vol. 11, no. 3, pp. 736–741, 2002, doi: https://doi.org/10.1016/S0925-9635(01)00561-1.

[5] Y. Berthier, “Maurice Godet’s Third Body,” in *The Third Body Concept Interpretation of Tribological Phenomena*, vol. 31, D. Dowson, C. M. Taylor, T. H. C. Childs, G. Dalmaz, Y. Berthier, L. Flamand, J.-M. Georges, and A. A. B. T.-T. S. Lubrecht, Eds. Elsevier, 1996, pp. 21–30.

[6] N. Fillot, I. Iordanoff, and Y. Berthier, “Modelling third body flows with a discrete element method—a tool for understanding wear with adhesive particles,” *Tribol. Int.*, vol. 40, no. 6, pp. 973–981, 2007, doi: https://doi.org/10.1016/j.triboint.2006.02.056.

[7] N. Fillot, I. Iordanoff, and Y. Berthier, *Simulation of Wear Through Mass Balance in a Dry Contact*, vol. 127. 2004.

[8] J. Konstanty, “Chapter 2 - Machining with diamonds — Theoretical model,” J. B. T.-P. M. D. T. Konstanty, Ed. Amsterdam: Elsevier Science, 2005, pp. 21–38.

[9] A. Ersoy, S. Buyuksagic, and U. Atici, “Wear characteristics of circular diamond saws in the cutting of different hard abrasive rocks,” *Wear*, vol. 258, no. 9, pp. 1422–1436, 2005, doi: https://doi.org/10.1016/j.wear.2004.09.060.

[10] M. Mostofi, T. Richard, L. Franca, and S. Yalamanchi, “Wear response of impregnated diamond bits,” *Wear*, vol. 410–411, pp. 34–42, 2018, doi: https://doi.org/10.1016/j.wear.2018.04.010.

[11] J. Konstanty, “Theoretical analysis of stone sawing with diamonds,” *J. Mater. Process. Technol.*, vol. 123, no. 1, pp. 146–154, 2002, doi: https://doi.org/10.1016/S0924-0136(02)00071-7.

[12] J. Konstanty, T. Kim, and S.-B. Kim, “Resistance to Abrasive Wear of Materials Used as Metallic Matrices in Diamond Impregnated Tools,” *Mater. Sci. Forum - MATER SCI FORUM*, vol. 534–536, pp. 1125–1128, Jan. 2007, doi: 10.4028/www.scientific.net/MSF.534-536.1125.

[13] E. Rabinowicz and A. Mutis, “Effect of abrasive particle size on wear,” *Wear*, vol. 8, no. 5, pp. 381–390, 1965, doi: https://doi.org/10.1016/0043-1648(65)90169-9.

[14] J. Konstanty, “Chapter 7 - Wear properties of the matrix,” J. B. T.-P. M. D. T. Konstanty, Ed. Amsterdam: Elsevier Science, 2005, pp. 113–127.

[15] I. Ucun, K. Aslantas, I. S. Buyuksagis, and S. Tasgetiren, “An investigation on the effect of diamond concentration and matrix material composition in the circular sawing process of granites,” *Proc. Inst. Mech. Eng. Part C-journal Mech. Eng. Sci. - PROC INST MECH ENG C-J MECH E*, vol. 1, pp. 1–11, Jan. 2010, doi: 10.1243/09544062JMES2104.

[16] D. N. Wright, H. Wapler, and H. K. Tönshoff, “Investigations and Prediction of Diamond Wear when Sawing,” *CIRP Ann.*, vol. 35, no. 1, pp. 239–244, 1986, doi: https://doi.org/10.1016/S0007-8506(07)61879-4.

[17] X. Zhao and L. Duan, “A Review of the Diamond Retention Capacity of Metal Bond Matrices,” *Metals (Basel).*, vol. 8, p. 307, Apr. 2018, doi: 10.3390/met8050307.

[18] J. Borowiecka-jamrozek and J. Lachowski, “An Analysis of the Retention of a Diamond Particle in a Metallic Matrix after Hot Pressing,” *Arch. Foundry Eng.*, vol. 17, Mar. 2017, doi: 10.1515/afe-2017-0003.

[19] S. W. Webb, “Diamond retention in sintered cobalt bonds for stone cutting and drilling,” *Diam. Relat. Mater.*, vol. 8, no. 11, pp. 2043–2052, 1999, doi: https://doi.org/10.1016/S0925-9635(99)00167-3.

[20] J. F. Archard, “Contact and Rubbing of Flat Surfaces,” *J. Appl. Phys.*, vol. 24, no. 8, pp. 981–988, Aug. 1953, doi: 10.1063/1.1721448.

[21] M. T. Siniawski, S. J. Harris, and Q. Wang, “A universal wear law for abrasion,” *Wear*, vol. 262, no. 7–8, pp. 883–888, 2007, doi: 10.1016/j.wear.2006.08.017.

[22] S. J. Bull and D. S. Rickerby, “Multi-pass scratch testing as a model for abrasive wear,” *Thin Solid Films*, vol. 181, no. 1, pp. 545–553, 1989, doi: https://doi.org/10.1016/0040-6090(89)90523-3.

[23] T. Kayaba, K. Hokkirigawa, and K. Kato, “Analysis of the abrasive wear mechanism by successive observations of wear processes in a scanning electron microscope,” *Wear*, vol. 110, no. 3, pp. 419–430, 1986, doi: https://doi.org/10.1016/0043-1648(86)90115-8.

[24] W. Brostow, G. Darmarla, J. Howe, and D. Pietkiewicz, “Determination of wear of surfaces by scratch testing,” *E-Polymers*, no. 025, pp. 1–8, 2004, doi: 10.1515/epoly.2004.4.1.255.

[25] M. Woldman, E. Van Der Heide, T. Tinga, and M. A. Masen, “A Finite Element Approach to Modeling Abrasive Wear Modes,” *Tribol. Trans.*, vol. 60, no. 4, pp. 711–718, 2017, doi: 10.1080/10402004.2016.1206647.

[26] A. Misra and I. Finnie, “On the size effect in abrasive and erosive wear,” *Wear*, vol. 65, no. 3, pp. 359–373, 1981, doi: https://doi.org/10.1016/0043-1648(81)90062-4.

[27] D. V De Pellegrin and G. W. Stachowiak, “Assessing the role of particle shape and scale in abrasion using ‘sharpness analysis’: Part II. Technique evaluation,” *Wear*, vol. 253, no. 9, pp. 1026–1034, 2002, doi: https://doi.org/10.1016/S0043-1648(02)00233-8.

[28] D. V. De Pellegrin and G. W. Stachowiak, “Simulation of three-dimensional abrasive particles,” *Wear*, vol. 258, no. 1-4 SPEC. ISS., pp. 208–216, 2005, doi: 10.1016/j.wear.2004.09.040.

[29] G. B. Stachowiak and G. W. Stachowiak, “The effects of particle characteristics on three-body abrasive wear,” *Wear*, vol. 249, no. 3–4, pp. 201–207, 2001, doi: 10.1016/S0043-1648(01)00557-9.

[30] M. Woldman, E. Van Der Heide, T. Tinga, and M. A. Masen, “The influence of abrasive body dimensions on single asperity wear,” *Wear*, vol. 301, no. 1–2, pp. 76–81, 2013, doi: 10.1016/j.wear.2012.12.009.

[31] Y. Zhou, P. D. Funkenbusch, and D. J. Quesnel, “Stress distributions at the abrasive - matrix interface during tool wear in bound abrasive grinding - a finite element analysis,” *Wear*, vol. 209, no. 1–2, pp. 247–254, 1997, doi: 10.1016/S0043-1648(96)07490-X.

[32] B. Li, P. M. Amaral, L. Reis, C. A. Anjinho, L. G. Rosa, and M. de Freitas, “3D-modelling of the local plastic deformation and residual stresses of PM diamond-metal matrix composites,” *Comput. Mater. Sci.*, vol. 47, no. 4, pp. 1023–1030, 2010, doi: 10.1016/j.commatsci.2009.12.001.

[33] C. M. Suh, K. S. Bae, and M. S. Suh, “Wear behavior of diamond wheel for grinding optical connector ferrule - FEA and wear test - FEA a,” *J. Mech. Sci. Technol.*, vol. 22, no. 11, pp. 2009–2015, 2008, doi: 10.1007/s12206-008-0407-8.

[34] J. Xu, A. H. Sheikh, and C. Xu, “3-D Finite element modelling of diamond pull-out failure in impregnated diamond bits,” *Diam. Relat. Mater.*, vol. 71, pp. 1–12, 2017, doi: 10.1016/j.diamond.2016.11.006.

[35] A. Deborde and T. Commeau, “Design of high performance binder by understanding the protrusion and clearance dynamics of diamonds during the cutting process,” Internal report from the company Umicore Specialty Powders France, 2017.

[36] T. Commeau, A. Nouveau, and A. Deborde, “Usure de matrices métalliques dans un flux de debris,” Internal report from the company Umicore Specialty Powders France, pp. 1–11, 2017.

[37] D. Dowson, “A generalized Reynolds equation for fluid-film lubrication,” *Int. J. Mech. Sci.*, vol. 4, no. 2, pp. 159–170, 1962, doi: https://doi.org/10.1016/S0020-7403(62)80038-1.

[38] O. Reynolds, “On the Theory of Lubrication and Its Application to Mr. Lowe’s Experiments,” *Philos. Trans. R. Soc. London*, vol. 177, pp. 157–234, 1886, [Online]. Available: https://scholar.google.com/scholar?q=related:zTMHxlMaYncJ:scholar.google.com/&hl=en&as_sdt=0,39&as_ylo=1886&as_yhi=1886#0.

[39] I. Hutchings and P. Shipway, “6 - Wear by hard particles,” I. Hutchings and P. B. T.-T. (Second E. Shipway, Eds. Butterworth-Heinemann, 2017, pp. 165–236.

[40] R. Jaza, G. Mollon, S. Descartes, A. Paquet, and Y. Berthier, “Lessons learned using machine learning to link third body particles morphology to interface rheology,” *Tribol. Int.*, vol. 153, p. 106630, 2021, doi: https://doi.org/10.1016/j.triboint.2020.106630.

[41] G. Mollon, V. Richefeu, P. Villard, and D. Daudon, “Discrete modelling of rock avalanches: sensitivity to block and slope geometries,” *Granul. Matter*, vol. 17, no. 5, pp. 645–666, 2015, doi: 10.1007/s10035-015-0586-9.

[42] G. Mollon, A. Quacquarelli, E. Andò, and G. Viggiani, “Can friction replace roughness in the numerical simulation of granular materials?,” *Granul. Matter*, vol. 22, no. 2, p. 42, 2020, doi: 10.1007/s10035-020-1004-5.

[43] G. W. Stachowiak, “Particle angularity and its relationship to abrasive and erosive wear,” *Wear*, vol. 241, no. 2, pp. 214–219, 2000, doi: https://doi.org/10.1016/S0043-1648(00)00378-1.

[44] M. Woldman, E. van der Heide, D. J. Schipper, T. Tinga, and M. A. Masen, “Investigating the influence of sand particle properties on abrasive wear behaviour,” *Wear*, vol. 294–295, pp. 419–426, 2012, doi: https://doi.org/10.1016/j.wear.2012.07.017.

[45] K. Kato, K. Hokkirigawa, T. Kayaba, and Y. Endo, “Three dimensional shape effect on abrasive wear,” *J. Tribol.*, vol. 108, no. 3, pp. 346–349, 1986.

[46] G. Mollon and J. Zhao, “Fourier–Voronoi-based generation of realistic samples for discrete modelling of granular materials,” *Granul. Matter*, vol. 14, pp. 621–638, Sep. 2012, doi: 10.1007/s10035-012-0356-x.

[47] M. G. Gee, A. Gant, and L. Van der Berg, “Fine scale abrasion testing of hardmetals and ceramics,” 1999.

[48] M. G. Gee, “Low load multiple scratch tests of ceramics and hard metals,” *Wear*, vol. 250, no. 1, pp. 264–281, 2001, doi: https://doi.org/10.1016/S0043-1648(01)00591-9.

[49] C. Gauthier, S. Lafaye, and R. Schirrer, “Elastic recovery of a scratch in a polymeric surface: experiments and analysis,” *Tribol. Int.*, vol. 34, no. 7, pp. 469–479, 2001, doi: https://doi.org/10.1016/S0301-679X(01)00043-3.

[50] C. Gear, “The Numerical Integration of Ordinary Differential Equations of Various Orders,” *Math. Comput.*, vol. 21, May 1969, doi: 10.2307/2004155.

[51] J. R. Cash, “On the integration of stiff systems of O.D.E.s using extended backward differentiation formulae,” *Numer. Math.*, vol. 34, no. 3, pp. 235–246, 1980, doi: 10.1007/BF01396701.

[52] P. K. Senapati, D. Panda, and A. Parida, “Predicting Viscosity of Limestone-Water Slurry,” *J. Miner. Mater. Charact. Eng.*, vol. 08, Jan. 2009, doi: 10.4236/jmmce.2009.83018.

[53] S. K. Mishra, P. K. Senapati, and D. Panda, “Rheological Behavior of Coal-Water Slurry,” *Energy Sources*, vol. 24, no. 2, pp. 159–167, Feb. 2002, doi: 10.1080/00908310252774471.

[54] C. Dorier and J. Tichy, “Behavior of a bingham-like viscous fluid in lubrication flows,” *J. Nonnewton. Fluid Mech.*, vol. 45, no. 3, pp. 291–310, 1992, doi: https://doi.org/10.1016/0377-0257(92)80065-6.

[55] I. A. Frigaard and C. Nouar, “On the usage of viscosity regularisation methods for visco-plastic fluid flow computation,” *J. Nonnewton. Fluid Mech.*, vol. 127, no. 1, pp. 1–26, 2005, doi: https://doi.org/10.1016/j.jnnfm.2005.01.003.

[56] T. C. Papanastasiou, “Flows of Materials with Yield,” *J. Rheol. (N. Y. N. Y).*, vol. 31, no. 5, pp. 385–404, Jul. 1987, doi: 10.1122/1.549926.

[57] M. Ö. Bora, O. Coban, T. Sinmazcelik, V. Günay, and M. Zeren, “Instrumented indentation and scratch testing evaluation of tribological properties of tin-based bearing materials,” *Mater. Des.*, vol. 31, no. 6, pp. 2707–2715, 2010, doi: 10.1016/j.matdes.2010.01.033.

[58] K. Hokkirigawa, K. Kato, and Z. Z. Li, “The effect of hardness on the transition of the abrasive wear mechanism of steels,” *Wear*, vol. 123, no. 2, pp. 241–251, 1988, doi: https://doi.org/10.1016/0043-1648(88)90102-0.

[59] N. Cane and J. Skinner, “N. CANE and J. SKINNER* Physics and Chemistry of Solids, Ca~e~dis~ Laboratory, University of Cambridge (Gt. Britain) (Received January 4, 1973),” *Physics (College. Park. Md).*, vol. 24, pp. 207–217, 1973.

[60] S. Graça, R. Colaço, and R. Vilar, “Micro-to-nano indentation and scratch hardness in the Ni-Co system: Depth dependence and implications for tribological behavior,” *Tribol. Lett.*, vol. 31, no. 3, pp. 177–185, 2008, doi: 10.1007/s11249-008-9350-1.

[61] A. Kareer, X. D. Hou, N. M. Jennett, and S. V. Hainsworth, “The interaction between Lateral size effect and grain size when scratching polycrystalline copper using a Berkovich indenter,” *Philos. Mag.*, vol. 96, no. 32–34, pp. 3414–3429, 2016, doi: 10.1080/14786435.2016.1240881.

[62] J.-F. Ferellec and G. McDowell, “A simple method to create complex particle shapes for DEM,” *Geomech. Geoengin. An Int. J.*, vol. 3, pp. 211–216, Sep. 2008, doi: 10.1080/17486020802253992.

[63] D. V De Pellegrin and G. W. Stachowiak, “Sharpness of abrasive particles and surfaces,” *Wear*, vol. 256, no. 6, pp. 614–622, 2004, doi: https://doi.org/10.1016/j.wear.2003.10.004.